Front. Mech. Eng. 2023, 18(1): 9
https://doi.org/10.1007/s11465-022-0725-z

RESEARCH ARTICLE

# Iterative HOEO fusion strategy: a promising tool for enhancing bearing fault feature

**Xingxing JIANG[a], Demin PENG[a], Jianfeng GUO[b], Jie LIU[c], Changqing SHEN[a], Zhongkui ZHU (✉)[a]**

[a] *School of Rail Transportation, Soochow University, Suzhou 215131, China*
[b] *China Academy of Railway Sciences Co. Ltd., Beijing 100094, China*
[c] *School of Civil and Hydraulic Engineering, Huazhong University of Science and Technology, Wuhan 430074, China*
✉ *Corresponding author. E-mail: zhuzhongkui@suda.edu.cn (Zhongkui ZHU)*



**ABSTRACT** As parameter independent yet simple techniques, the energy operator (EO) and its variants have received considerable attention in the field of bearing fault feature detection. However, the performances of these improved EO techniques are subjected to the limited number of EOs, and they cannot reflect the non-linearity of the machinery dynamic systems and affect the noise reduction. As a result, the fault-related transients strengthened by these improved EO techniques are still subject to contamination of strong noises. To address these issues, this paper presents a novel EO fusion strategy for enhancing the bearing fault feature nonlinearly and effectively. Specifically, the proposed strategy is conducted through the following three steps. First, a multi-dimensional information matrix (MDIM) is constructed by performing the higher order energy operator (HOEO) on the analysis signal iteratively. MDIM is regarded as the fusion source of the proposed strategy with the properties of improving the signal-to-interference ratio and suppressing the noise in the low-frequency region. Second, an enhanced manifold learning algorithm is performed on the normalized MDIM to extract the intrinsic manifolds correlated with the fault-related impulses. Third, the intrinsic manifolds are weighted to recover the fault-related transients. Simulation studies and experimental verifications confirm that the proposed strategy is more effective for enhancing the bearing fault feature than the existing methods, including HOEOs, the weighting HOEO fusion, the fast Kurtogram, and the empirical mode decomposition.

**KEYWORDS** higher order energy operator, fault diagnosis, manifold learning, rolling element bearing, information fusion

## 1 Introduction

Rolling element bearings (REBs) are widely used in rotating machinery, and their failure is an important cause of mechanical breakdowns and accidents [1,2]. Therefore, the diagnosis of the early fault of REBs plays a vital role in ensuring the safety of the rotating machinery and guaranteeing its normal performance [3,4]. However, owing to the interference of strong background noise and suboptimal scenario in practical engineering, the fault diagnosis of REBs remains a challenging issue [5]. Vibration signals collected from the rotating machinery are known to carry useful diagnosis information of REBs. The symptomatic signatures with the repetitive transients are contained to indicate the occurrence of a defect. As a result, various specific signal processing techniques dedicated to the recovery of repetitive transients have been developed in the past few decades. Examples of such techniques include wavelet-based methods [6,7], sparsity-based methods [8,9], stochastic resonance [10–12], and adaptive signal decomposition [13–17]. However, some of these methods still have room for improvement in analyzing vibration data with strong interference.

The design of suitable parameters in detecting resonance bands excited by defects of REBs is easily influenced by the change of operating environments. Thus, Liang and Bozchalooi [18] first proposed a non-resonance-based method using an energy operator (EO) for the online health monitoring of REBs in industrial environments. As non-resonance methods with a free parameter, EO and its recycling application with limited numbers are effective for enhancing the signal-to-interference ratio (SIR) of the original signal.

*Received February 13, 2022; accepted July 28, 2022*

Subsequently, various studies employed EO as a pre/post-processing technique to enhance the fault feature buried in the originally collected vibration signals [19,20] or the fault-related modes of REBs extracted by adaptive decomposition methods [21–25]. Moreover, as an alternative technique of Hilbert transform, EO is also typically used as a demodulation tool to extract the instantaneous frequency or/and amplitude for the fault diagnosis of REBs [26–28]. However, Randall and Smith [29] pointed out that replacing the EO with the squared envelope of the derivative of a signal using non-causal techniques applied in the frequency domain for the vast majority of applications in machine diagnostics can have a considerable advantage, particularly for the estimation of the instantaneous frequency.

In view of the ability of the strong interference suppression of EO, some of its variant versions are further presented to detect the early fault feature of REBs. For instance, the amplitude demodulation differentiation method [30], which is performed by a differentiated operation after the amplitude demodulation, is presented to eliminate the high-amplitude low-frequency vibration interferences. A calculus-enhanced EO [31] is constructed to enhance the noise suppression ability for which an integration operator is incorporated into the EO. A frequency-weighted EO is defined for the fault detection of REBs [32,33], which has a similar result with EO as verified in Ref. [29]. Moreover, our group presents the usage of the multi-resolution EO to avoid the negative value phenomenon of EO, which could also be regarded as an expanded version of the calculus-enhanced EO in Ref. [34]. Recently, the higher order energy operator (HOEO) was introduced for estimating the instantaneous frequency and amplitude to obtain a fine fault feature of rotating machinery. As a generalization of EO, the HOEO not only inherits the merits of EO but also has higher precision and better robustness to noise [35,36]. However, the essence of the transformations of EO and its variants is to increase the weighting with frequency for each component. As a result, EO and its variants may also amplify the higher frequency noise and interferences, which can adversely impact the effectiveness of EO and its variants. Moreover, predicting which order of EO will yield the optimal result is difficult. Faghidi and Liang [37,38] proposed the strategy of weighting higher order energy operator fusion (WHOEOF), which takes the result from each HOEO as a distinct dataset from a virtual sensor and then linearly weights multiple HOEOs as the fused result.

In summary, the fusion strategy is reasonable to have a canceling effect of the random noise by averaging different HOEOs. However, two reasons might hinder the noise reduction effect of the strategy of WHOEOF. (1) Only a few orders of HOEOs are fed into the fused result because of the increase of high-frequency noise in the process of applying multiple differentiations. Hence, the enhanced results of the fusion strategies are subjected to the limited numbers of HOEOs. (2) The strategy of WHOEOF extracts the fault-related feature by linearly combining the HOEOs at different orders guided by maximizing the information measure. Thus, the strategy of WHOEOF could not reflect the non-linearity of the machinery dynamic systems and affects the noise reduction. To address the issues mentioned above, this paper presents an iterative HOEO fusion strategy to remove the amplified noise contained in the results of HOEOs effectively to enhance the REB fault feature. The main contributions of the proposed strategy are as follows:

(1) Reference [18] verified that the recycle operation is also effective for improving the SIR of the analysis signal. Therefore, the recycle application of HOEOs is used to enrich the fusion input for remedying the deficiency of a few numbers of HOEOs in the proposed strategy. Consequently, a multi-dimensional information matrix (MDIM) that contains the enhanced fault feature of REBs is constructed by combining the HOEOs and their iterative results.

(2) The enhanced manifold learning method is designed to fuse the constructed MDIM nonlinearly for excellently extracting the intrinsic transients related to the bearing defects. Meanwhile, the eigenvalue weighting idea is used to combine the main manifolds for recovering the complete impulsive structure of the fault-related features. As a result, the proposed iterative HOEO fusion strategy is completely different from the current linearly weighting fusion to wipe off the influence of amplified high-frequency noise in the HOEOs and their iterative results.

This paper is organized as follows. Section 2 introduces the theoretical background, including EO, HOEO, and their linearly weighting fusion. In Section 3, the iterative HOEO fusion strategy for enhancing the REB fault feature is described in detail. Section 4 gives the simulated cases to validate the proposed strategy. In Section 5, three experimental cases are conducted to verify the effectiveness of the proposed strategy. Finally, the main conclusions are given in Section 6.

## 2 Description of EO and its variants

### 2.1 EO and its characteristics

The EO is originally presented for non-linear speech processing and called Teager–Kaiser energy operator [31]. The definition of EO for a continuous time signal $x(t)$ is as follows:

$$\mathrm{E}_2[x(t)] = (\dot{x}(t))^2 - x(t)\ddot{x}(t), \tag{1}$$

where $\dot{x}(t)$ and $\ddot{x}(t)$ are the first- and second-order derivatives of $x(t)$ with respect to time $t$, respectively.

Thus, the discrete form of the EO is given as follows:

$$\mathrm{E}_2[x(n)] = (x(n))^2 - x(n+1)x(n-1), \tag{2}$$

where $x(n)_{n=1,2,\ldots,N}$ is the discrete form of $x(t)$, $n$ is the $n$th point of $x(t)$.

Some characteristics of EO have been revealed in current studies. Reference [18] validated that the SIR of the bearing signal with multiple vibration interferences $x(t) = r(t) + \sum_{j=1}^{K} u_j(t)$ could be enhanced by using the transformation of EO. The definition of the SIR in the context of bearing fault detection is given as follows [18]:

$$\mathrm{SIR}(x(t)) = \frac{\frac{1}{T}\int_0^T r^2(t)\,\mathrm{d}t}{\frac{1}{T}\int_0^T \sum_{j=1}^{K} u_j^2(t)\mathrm{d}t}, \tag{3}$$

where $r(t) = A\mathrm{e}^{-\beta}\cos(\omega_\mathrm{r} t + \varphi)$ is the fault bearing vibration, $u_j(t) = L_j \cos\omega_j t$ stands for multiple vibration interferences, $T$ is the time period of the fault bearing vibration, $K$ is the total number of the vibration interferences, $A$ is the amplitude of the fault bearing vibration, $\beta$ is the structural damping characteristic of the fault bearing vibration, $\omega_\mathrm{r}$ is the resonance frequency excited by the bearing defect, $\varphi$ is the phase of the fault bearing vibration, $L_j$ denotes the amplitude of the $j$th interference component, and $\omega_j$ represents the frequency of the $j$th interference component. Under some assumptions [18], the SIRs of $x(t)$ and its EO are derived as follows:

$$\mathrm{SIR}(x(t)) \approx \begin{cases} \dfrac{3A^2}{4T_\mathrm{p}\beta\sum_{j=1}^{K} L_j^2}, & \beta \approx \omega_\mathrm{r}, \\ \dfrac{A^2}{2T_\mathrm{p}\beta\sum_{j=1}^{K} L_j^2}, & \beta \ll \omega_\mathrm{r}, \end{cases} \tag{4}$$

and

$$\mathrm{SIR}(\mathrm{E}_2[x(t)]) \approx \frac{A^4\omega_\mathrm{r}^4}{4T_\mathrm{p}\beta\sum_{j=1}^{K} L_j^4\omega_j^4}, \tag{5}$$

where $T_\mathrm{p}$ is the time period of the fault characteristic frequency.

By combining Eqs. (4) and (5), the ratio of SIRs between EO and the raw signal can be made as follows [18]:

$$\frac{\mathrm{SIR}(\mathrm{E}_2[x(t)])}{\mathrm{SIR}(x(t))} \approx \begin{cases} \dfrac{\sum_{j=1}^{K} L_j^2 A^2 \omega_\mathrm{r}^4}{3\sum_{j=1}^{K} L_j^4\omega_j^4}, & \beta \approx \omega_\mathrm{r}, \\ \dfrac{\sum_{j=1}^{K} L_j^2 A^2 \omega_\mathrm{r}^4}{2\sum_{j=1}^{K} L_j^4\omega_j^4}, & \beta \ll \omega_\mathrm{r}. \end{cases} \tag{6}$$

Considering that the resonance frequency is usually much higher than interference signal frequency, that is, $\omega_\mathrm{r} \gg \omega_j$, and strong interferences exist in the bearing signal, that is, $L_j > A$, the SIR of the signal obtained by EO is generally higher than that of the raw signal:

$$\mathrm{SIR}(\mathrm{E}_2[x(t)]) > \mathrm{SIR}(x(t)). \tag{7}$$

According to the conclusion in Eq. (7), we can directly obtain the following:

$$\mathrm{SIR}(\mathrm{E}_2[\mathrm{E}_2[x(t)]]) > \mathrm{SIR}(\mathrm{E}_2[x(t)]), \tag{8}$$

for which $\mathrm{E}_2[x(t)]$ is regarded as a new input signal. Therefore, the component of the faulty bearing vibration can be further enhanced by recycling the EO on the transformed signal.

Moreover, given the proven result in Ref. [29], the EO is equivalent to the squared envelope of $\dot{x}(t)$ as follows:

$$\mathrm{E}_2[x(t)] \approx \mathrm{Envsq}[\dot{x}(t)], \tag{9}$$

where $\mathrm{Envsq}[\dot{x}(t)]$ is expressed by

$$\mathrm{Envsq}[\dot{x}(t)] = (\dot{x}(t))^2 + \left(\hat{\dot{x}}(t)\right)^2, \tag{10}$$

where $\hat{\dot{x}}(t)$ is the Hilbert transform of $\dot{x}(t)$. The Fourier transform of $\dot{x}(t)$ is that of $x(t)$ by simply multiplying with $\mathrm{i}\omega$. Thus, Ref. [29] concluded that any benefit coming from the EO can be attributed to the differentiation of the signal, giving a weighting of the spectrum proportional to frequency. However, the relative strength of the noise in the high-frequency region is also amplified simultaneously.

### 2.2 HOEO and its linearly weighting fusion

As an extension of EO, the definition of HOEO for signal $x(t)$ is as follows [39]:

$$\mathrm{E}_j[x(t)] = \dot{x}(t)x^{(j-1)}(t) - x(t)x^{(j)}(t), \tag{11}$$

and its discrete form is given as follows:

$$\mathrm{E}_j[x(n)] = x(n)x(n+j-2) - x(n-1)x(n+j-1), \tag{12}$$

where $x^{(j)}(t)$ is the $j$th derivative of $x(t)$.

Reference [37] used the ratio between the SIR of the fourth-order EO and that of the EO of the bearing signal with multiple vibration interferences as an example for

explaining the merit of HOEO for enhancing the SIR as follows:

$$\frac{\mathrm{SIR}\left(\mathrm{E}_4\left[x(t)\right]\right)}{\mathrm{SIR}\left(\mathrm{E}_2\left[x(t)\right]\right)} \approx \frac{\omega_{\mathrm{r}}^4 \sum_{j=1}^{K}\left(L_j^4\omega_j^4\right)}{\sum_{j=1}^{K}\left(L_j^4\omega_j^8\right)}. \tag{13}$$

As shown in the above equation, given that the interference frequency $\omega_j$ is usually much lower than the resonance frequency $\omega_{\mathrm{r}}$, the SIR of the fourth-order EO is much higher than that of the EO. Thus, the bearing fault-related information can be further strengthened by applying an HOEO. However, the relative intensity of high-frequency noise might be dramatically amplified when the HOEO processes the signal. Moreover, predicting the best order of HOEO is difficult. Thus, Ref. [37] constructed the strategy of WHOEOF by recognizing multiple HOEOs as data sets collected from different virtual sensors as follows:

$$\text{HOEO-F}\left[x(t)\right] = \sum_{j=2}^{J}\left\{\alpha_j \mathrm{E}_j\left[x(t)\right]\right\}, \tag{14}$$

where $J$ is the total number of orders and $\alpha_j$ is the coefficient associated with order $j$ of HOEO. As a result, a set of optimal coefficients $\boldsymbol{\alpha}^* = \left[\alpha_1^*, ..., \alpha_j^*, ..., \alpha_J^*\right]$ are obtained by maximizing the kurtosis of HOEO-F$(x(n))$ as follows:

$$\boldsymbol{\alpha}^* = \arg\max_{\alpha}\left(\mathrm{Kurt}\left(\text{HOEO-F}\left[x(t)\right]\right)\right), \tag{15}$$

where $\boldsymbol{\alpha} = [\alpha_1, ..., \alpha_j, ..., \alpha_J]$ and Kurt$(\cdot)$ is the function of kurtosis.

## 3 Proposed iterative HOEO fusion strategy for the bearing fault diagnosis

The current strategy of WHOEOF is devoted to eliminating the random noise with a high-frequency by averaging multiple HOEOs. In addition, the SIR of the WHOEOF result is further enhanced by taking advantage of the contribution of each HOEO. However, only the limited numbers of HOEOs could be used as the sources of fusion because of the evident enhancement of high-frequency noise with the increase of the order of HOEO. Thus, the noise suppression effect will not be evident only by averaging the limited numbers of HOEOs. Moreover, the noise reduction is restricted to the operation of linearly weighting fusion as the nonlinear property usually exists in the collected signal from the machinery dynamic systems. Considering the above-discussed issues, an iterative HOEO fusion strategy is presented for enhancing the bearing fault feature in this section. First, we construct an MDIM by performing iterative HOEO to provide plentiful sources for the fusion operation in Subsection 3.1. Then, the enhanced manifold learning is designed to synthesize the information of MDIM nonlinearly for extracting the fault-related transient in Subsection 3.2. Lastly, the procedure of the proposed iterative HOEO fusion strategy for the bearing fault diagnosis is described in Subsection 3.3.

### 3.1 Construction of MDIM by performing iterative HOEO

As mentioned above, the recycling application of the EO is also beneficial to the improvement of the component of the fault bearing vibration. Therefore, the number of HOEOs can be doubled by performing the recycling application of the EO on the HOEOs, that is, iterative HOEO without incorporating excessive differentiate operations, to compensate for the deficiency of the limited number of HOEOs in the fusion result. Specifically, the construction of MDIM is given as follows.

The number $J$ of the HOEOs is first formulated as a matrix $\boldsymbol{M}_1(x(t))_{t\in[0,T]}$:

$$\boldsymbol{M}_1\left[x(t)\right]_{t\in[0,T]} = \begin{bmatrix} \mathrm{E}_2\left[x(t)\right] \\ \vdots \\ \mathrm{E}_j\left[x(t)\right] \\ \vdots \\ \mathrm{E}_J\left(x(t)\right) \end{bmatrix}_{t\in[0,T]}, \tag{16}$$

where $T$ is the time length of the analysis signal and $J$ is the highest order of HOEO used in the MDIM. As shown in Ref. [37], the WHOEOF reaches an ideal result when the order $J$ is 6. Similarly, the same value of $J$ is used in our research to avoid the drawbacks induced by the excessive order and reduce the computational burden.

Then, iterative HOEO is performed on $\boldsymbol{M}_1(x(t))_{t\in[0,T]}$ as follows:

$$\boldsymbol{M}_2\left[x(t)\right] = \mathrm{E}_2\left[\boldsymbol{M}_1\left[x(t)\right]\right], \tag{17}$$

and

$$\boldsymbol{M}_3\left[x(t)\right] = \mathrm{E}_2\left[\boldsymbol{M}_2\left[x(t)\right]\right]. \tag{18}$$

Here, only two iterative operations are performed on $\boldsymbol{M}_1(x(t))_{t\in[0,T]}$ to avoid the effect on the HOEO with higher order in our study. The multiple iterations will dramatically amplify the high-frequency noise in the HOEO with higher order and also enlarge the difference among the impulses with different amplitudes, which will affect the final fusion result.

Finally, the MDIM by performing iterative HOEO is defined as follows:

$$\boldsymbol{M}\left[x(t)\right]_{t\in[0,T]} = \begin{bmatrix} \boldsymbol{M}_1\left[x(t)\right]_{t\in[0,T]} \\ \boldsymbol{M}_2\left[x(t)\right]_{t\in[0,T]} \\ \boldsymbol{M}_3\left[x(t)\right]_{t\in[0,T]} \end{bmatrix}. \tag{19}$$

For discrete signals, the MDIM is rewritten as follows:

$$\boldsymbol{M}[x(n)]_{n=1,2,...,N}=\begin{bmatrix}\boldsymbol{M}_1[x(n)]_{n=1,2,...,N}\\ \boldsymbol{M}_2[x(n)]_{n=1,2,...,N}\\ \boldsymbol{M}_3[x(n)]_{n=1,2,...,N}\end{bmatrix}, \tag{20}$$

where $\boldsymbol{M}_1[x(n)]_{n=1,2,...,N}$ is the discrete result of $\boldsymbol{M}_1[x(t)]_{t\in[0,T]}$ as

$$\boldsymbol{M}_1[x(n)]_{n=1,2,...,N}=\begin{bmatrix}\mathrm{E}_2[x(1)] & \cdots & \mathrm{E}_2[x(n)] & \cdots & \mathrm{E}_2[x(N)]\\ \vdots & & \vdots & & \vdots\\ \mathrm{E}_j[x(1)] & \cdots & \mathrm{E}_j[x(n)] & \cdots & \mathrm{E}_j[x(N)]\\ \vdots & & \vdots & & \vdots\\ \mathrm{E}_J[x(1)] & \cdots & \mathrm{E}_J[x(n)] & \cdots & \mathrm{E}_J[x(N)]\end{bmatrix}, \tag{21}$$

$\boldsymbol{M}_2[x(n)]=\mathrm{E}_2[\boldsymbol{M}_1[x(n)]]$, and $\boldsymbol{M}_3[x(n)]=\mathrm{E}_2[\boldsymbol{M}_2[x(n)]]$.

### 3.2 Enhanced manifold learning algorithm

Through the process of nonlinear dimensionality reduction, manifold learning can uncover the underlying structures of low-dimensional manifolds from high-dimensional data space. Its excellent de-noising performance has been validated in the fault feature extraction of rotating machinery [40–42]. Hence, this tool is promising for fusing the constructed MDIM to extract the intrinsic manifold with fault-related features. In recent years, various manifold learning algorithms have been presented, such as locality preserving projection, locally linear embedding, isometric mapping, Laplacian eigenmaps, and local tangent space alignment (LTSA) [40,41]. Owing to the merit of robustness to parameters and superiority in principal manifold reconstruction [43], the LTSA is introduced to fuse the constructed MDIM to reveal the intrinsic manifold feature in this research. The basic idea of LTSA is to use the local projections of the high-dimensional data on the tangent space to represent the low-dimensional manifolds. Then, these local tangent spaces are arranged to construct the manifold global coordinates. Specifically, the LTSA algorithm mainly includes the following three steps.

(1) Extract local information

MDIM $\boldsymbol{M}$ is given, that is, $\boldsymbol{M}[x(n)]_{n=1,2,...,N}$:

$$\boldsymbol{M}=[\boldsymbol{m}_1,...,\boldsymbol{m}_n,...,\boldsymbol{m}_N], \tag{22}$$

where $\boldsymbol{m}_n=\left[\boldsymbol{M}_1[x(n)]^{\mathrm{T}},\boldsymbol{M}_2[x(n)]^{\mathrm{T}},\boldsymbol{M}_3[x(n)]^{\mathrm{T}}\right]^{\mathrm{T}}$. Then, a set of $k$ nearest neighbors of column $\boldsymbol{m}_n$ is determined as $\boldsymbol{Z}_i$. Next, $\boldsymbol{Z}_i$ is centralized as $(\boldsymbol{Z}_i-\bar{\boldsymbol{Z}}_i(\boldsymbol{e}_k)^{\mathrm{T}})$, where $\bar{\boldsymbol{Z}}_i$ is the mean of $\boldsymbol{Z}_i$ and $\boldsymbol{e}_k$ is a column vector of $k$ ones. Consequently, the matrix $\boldsymbol{V}_i$ is formed via the $Id$ largest right singular vectors of centralized matrix $(\boldsymbol{Z}_i-\bar{\boldsymbol{Z}}_i(\boldsymbol{e}_k)^{\mathrm{T}})$.

(2) Construct alignment matrix

The 0-1 selection matrix $\boldsymbol{S}_i$ is determined through the information of $\boldsymbol{V}_i$ as follows:

$$\boldsymbol{S}_i=\boldsymbol{M}^{-1}\boldsymbol{V}_i. \tag{23}$$

Then, the correlation matrix $\boldsymbol{C}_i$ is computed as follows:

$$\boldsymbol{C}_i=\boldsymbol{I}-\left[\frac{\boldsymbol{e}_k}{\sqrt{k}}\quad\boldsymbol{V}_i\right]\left[\frac{\boldsymbol{e}_k}{\sqrt{k}}\quad\boldsymbol{V}_i\right]^{\mathrm{T}}, \tag{24}$$

where $\boldsymbol{I}$ is the identity matrix. As a result, the alignment matrix $\boldsymbol{A}$ is constructed as follows:

$$\boldsymbol{A}=\sum_{i=1}^{N}\left(\boldsymbol{S}_i\boldsymbol{C}_i\boldsymbol{C}_i^{\mathrm{T}}\boldsymbol{S}_i^{\mathrm{T}}\right). \tag{25}$$

(3) Obtain global representation

The $(Id+1)$ smallest eigenvalues and eigenvectors of the alignment matrix $\boldsymbol{A}$ are calculated, that is, $(\lambda_1,\lambda_2,\lambda_3,...,\lambda_{Id+1})$ and $(\boldsymbol{g}_1,\boldsymbol{g}_2,\boldsymbol{g}_3,...,\boldsymbol{g}_{Id+1})$. Then, the global representation $\boldsymbol{G}_0=(\boldsymbol{g}_2,\boldsymbol{g}_3,...,\boldsymbol{g}_{Id+1})$ is obtained by combining the eigenvectors from the second smallest one to the $(Id+1)$th smallest one.

Notably, $Id$ and $k$ are only two prior parameters in the manifold learning algorithm. The performance of LTSA is closely related to the two parameters. Parameter $Id$ is to determine the saved intrinsic dimensions. Generally, the value of $Id$ is far less than the original dimension of the MDIM ($\boldsymbol{M}$). Considering that some noises could exist in the global representation $\boldsymbol{G}_0$ with a large $Id$ and that some weak fault-related impulses might be omitted with a small $Id$, we set $Id$ as 3 in all cases of this study by trial and error. As only one-dimensional vector can be used to represent the final fusion result, the reorganizing result $\boldsymbol{G}$ of the global representation $\boldsymbol{G}_0$ with the eigenvalue weighting idea is conducted as follows:

$$\boldsymbol{G}=\frac{\sum_{i=2}^{Id+1}\pm\boldsymbol{g}_i}{\lambda_i\left\|\sum_{i=2}^{Id+1}\frac{\pm\boldsymbol{g}_i}{\lambda_i}\right\|_2}, \tag{26}$$

where $\lambda_i$ is the eigenvalue of $\boldsymbol{g}_i$. The reciprocal of the eigenvalue is used as the weighting coefficient because a big mapping error corresponds to an intrinsic eigenvector with a large eigenvalue [44]. Moreover, the plus or minus sign in Eq. (26) is determined according to the waveform of $\boldsymbol{g}_i$. Thus, the waveform of the final fusion result is as symmetrical as possible for obtaining a regular envelope spectrum.

Parameter $k$ determines the nearest neighboring size of each column of MDIM. Generally, an oversized $k$ of nearest neighbors will cause missing local information of the manifold structure. A very small value of $k$ will lead to a wrong result because of the singular of the matrix of the tangent space. A suitable one of $k$ must be searched to obtain an optimal fusing result. The widely used method is to maximize a measure for determining the size $k$ of the nearest neighbors. Sparsity measures [45] and complexity measures are two major categories to characterize the transients buried in the fault signal of rotating machinery. In sparsity measures, spectral kurtosis [46], negative entropy, smoothness index, and Gini index [47] have been thoroughly studied as objective functions to quantify

transients. Moreover, some novelty sparsity measures, such as Box-Cox sparse measures [48], generalized Gini indices [49], and measures constructed by quasi-arithmetic mean [50], have been proposed in recent years, for which the profound foundation has been provided by Wang et al. [48–51]. In complexity measures, correlation dimension, approximate entropy, dispersion entropy [52], diversity entropy [53], and permutation entropy (PE) [54] have been presented for characterizing the health conditions of rotating machinery. Various studies have verified that PE is a wonderful tool to evaluate the complexity of bearing vibration signal quantitatively [54]. Moreover, it has reliable performance for determining the parameters in LTSA [40–44]. Therefore, it is regarded as a criterion to determine an optimal $k^*$ in this study as follows:

$$k^* = \arg\min_k (PE_k), \tag{27}$$

where $PE_k$ is the PE of the reorganizing result $\boldsymbol{G}$ at the size $k$ of nearest neighbors.

$$PE_k = -\frac{\sum_{i=1}^{m!} (P_i \ln P)_i}{\ln(m!)}, \tag{28}$$

where $P_i$ is the relative frequency of $i$th permutation and $m$ is the embedded dimension set as 6 according to Ref. [54]. Undoubtedly, it is a very valuable research point with selecting or constructing an optimal measure for searching the size $k$ of nearest neighbors in the future research.

### 3.3 Procedure of iterative HOEO fusion strategy for enhancing bearing faulty feature

In summary, the procedure of the proposed iterative HOEO fusion strategy can be described briefly as follows.

Step 1: Construct the MDIM $\boldsymbol{M}$ by performing iterative HOEO on the analysis signal $x(t)$.

Step 2: Normalize the MDIM $\boldsymbol{M}$ to alleviate the effect of the high magnitude of impulses amplified by the HOEO as follows:

$$\overline{\boldsymbol{M}} = \left[\overline{\boldsymbol{R}}_1^{\mathrm{T}}, ..., \overline{\boldsymbol{R}}_i^{\mathrm{T}}, ..., \overline{\boldsymbol{R}}_{3\times J}^{\mathrm{T}}\right]^{\mathrm{T}}, \tag{29}$$

where $\overline{\boldsymbol{R}}_i$ is the normalized result of $\boldsymbol{R}_i$ of MDIM $\boldsymbol{M}$ as follows:

$$\overline{\boldsymbol{R}}_i = \frac{\boldsymbol{R}_i}{\|\boldsymbol{R}_i\|_2}. \tag{30}$$

Step 3: Utilize the enhanced manifold learning algorithm to extract the fused result from the normalized MDIM $\overline{\boldsymbol{M}}$.

Step 4: Observe the waveform and the envelope spectrum of the fused feature component to diagnose the health condition of the monitoring bearing.

Considering that manifold learning is a nonlinear de-noising method, the result of the iterative HOEO fusion strategy is the combination of multiple HOEOs and their iterative forms in a nonlinear way. Hence, the nonlinear repetitive transients can be well revealed from the constructed MDIM. Moreover, the weighting manifold representation with the reciprocal of the eigenvalue is designed to capture a comprehensive fusion in this study.

## 4 Simulation analysis

To verify the enhanced performance of the proposed strategy, a simulated bearing fault signal is constructed by considering the vibration characteristics of the bearing local defect as follows:

$$x(t) = \sum_i \mathrm{S}(t - iT_\mathrm{d} - \tau_i) + n(t), \tag{31}$$

where $\mathrm{S}(t) = \mathrm{e}^{-\xi t}\cos(2\pi f_{\mathrm{RE}} t)$ denotes a transient with unit amplitude imitated by an exponentially decaying cosinusoid, $f_{\mathrm{RE}}$ represents the resonance frequency, which is set as 1000 Hz, $\xi = 500$ specifies the decay rate of the transient, $T_\mathrm{d} = 0.02$ s is the time interval between two adjacent transients, $\tau_i$ simulates the slip effect of transients as a random variable that typically accounts for 1%–2% of the fault period with a zero-mean [55], $n(t)$ is the added noise component that is generated by the function "awgn ($y(t)$, signal-to-noise ratio (SNR), 'measured')", where $y(t)$ represents the preset transients and SNR is the expected value of signal-to-noise of the simulated signal. The sampling frequency of the simulated signal is set as 12000 Hz, and its lasting time is 0.2 s.

Here, the simulated signal with SNR = −8 dB is first selected to verify the proposed strategy. Figure 1 shows the time waveform and envelope spectrum of the simulated signal. The pure impulses are difficult to be identified from the waveform because of the corruption of the background noise. Moreover, the harmonics of fault-related frequency shown in the envelope spectrum are not evident. Then, the proposed strategy is used to analyze this simulated signal. The parameters used in the proposed strategy, including order $J$ of HOEO, the number of saved intrinsic dimensions $Id$, and the nearest neighboring size $k$ are determined according to the introduction given in Section 3. Specifically, the nearest neighboring size $k$ is optimized by the criterion of minimizing PE. Figure 2 draws the PE values of the fused results where the nearest neighboring size $k$ ranges from 10 to 40. As shown in Fig. 2, the PE gives a minimal value at $k = 34$, thereby being selected as the optimal nearest neighboring size to extract the final fused result. Figure 3 displays the time waveform and envelope spectrum of the final fused result. The heavy noise is

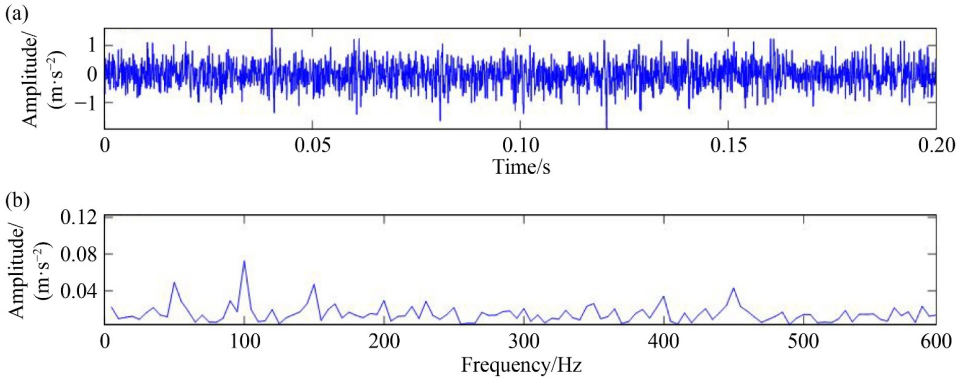


**Fig. 1** Simulated signal with SNR = −8 dB: (a) time waveform and (b) envelope spectrum.

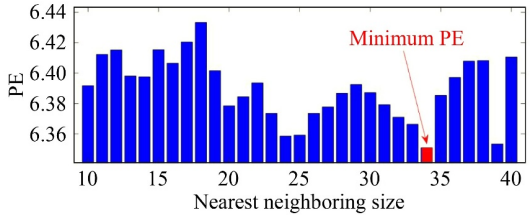


**Fig. 2** PE values of fused results of simulated signal under different nearest neighboring sizes. PE: permutation entropy.

almost totally wiped off, and the repetitive transients with the interval of $\Delta t_1 = 0.02$ s are exhibited clearly. Moreover, the envelope spectrum of the fused result shows the harmonics of fault-related frequency evidently. These results demonstrate the effectiveness of the proposed strategy.

Figure 4 shows the processing results of HOEOs with the orders from 2 to 6 as a comparison. Some transients are shown in the waveforms obtained by these HOEOs. Detecting the fault-related features is still difficult because of the absence of regular transients. Moreover, severe noise pollution still exists at these improved waveforms. For further comparison, the WHOEOF method proposed in Ref. [37] is used to process the same simulated signal. The parameters used in the WHOEOF method are identical to those given in Ref. [37]. Figure 5 shows the waveform and envelope spectrum of the fused result obtained by HOEO. Strong noise exists in the time waveform of the fused results. Moreover, the second harmonic of the fault-related frequency is more evident than itself. However, in sum, the fault-related frequency and its harmonics in the WHOEOF are not remarkable when comparing the results of the proposed strategy. The reason for this phenomenon is that reducing the contained noise by linearly weighting these HOEOs in the WHOEOF is difficult. All of this evidence indicates that the proposed strategy has a superior performance in enhancing the bearing fault feature.

To explore its robustness under a noisy environment further, the simulated signals with different SNRs are processed by the proposed iterative HOEO fusion strategy. Figure 6 shows the fused results of simulated signals with SNRs from –2 to –10 dB obtained by the proposed strategy. Notably, the optimal nearest neighboring size is used to extract the fused results with different SNRs. The simulated transients can be effectively identified under different SNRs situations. The residual noise in these fused results is reduced with the SNR increasing of the simulated signal. Therefore, the proposed iterative HOEO fusion strategy is quite suitable for enhancing the fault diagnosis of REB.

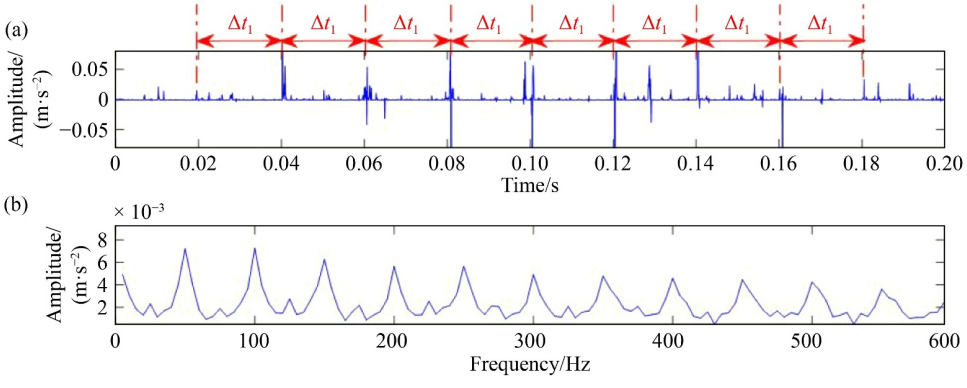


**Fig. 3** Fusion result of simulated signal obtained by the proposed strategy: (a) time waveform and (b) envelope spectrum.

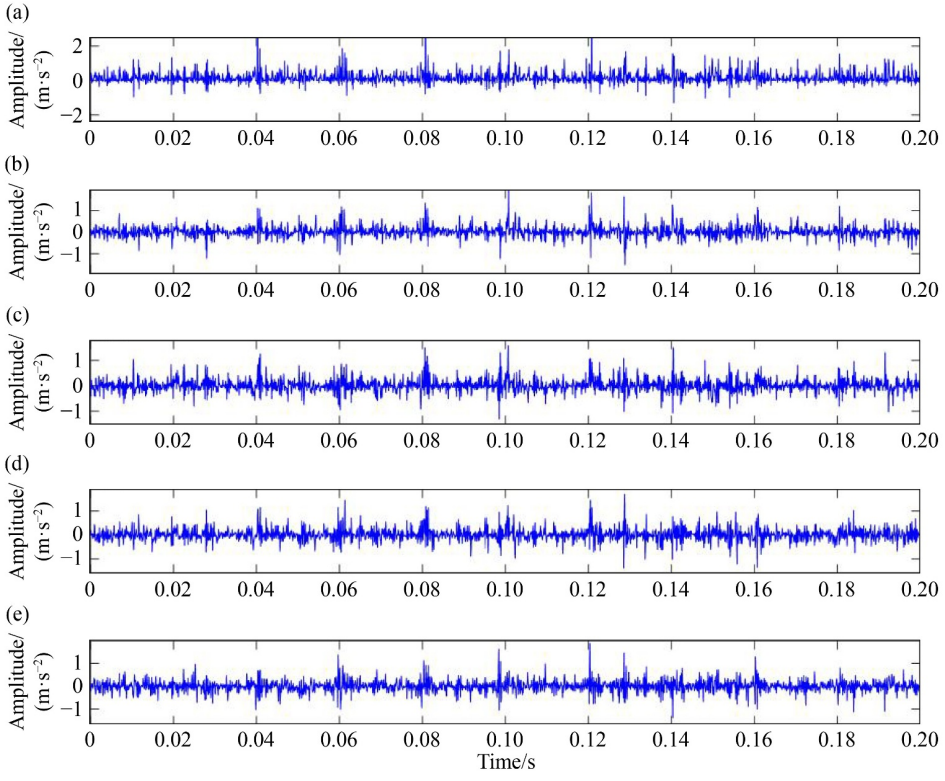


**Fig. 4** Results of higher order energy operators of simulated signal: (a) order 2, (b) order 3, (c) order 4, (d) order 5, and (e) order 6.

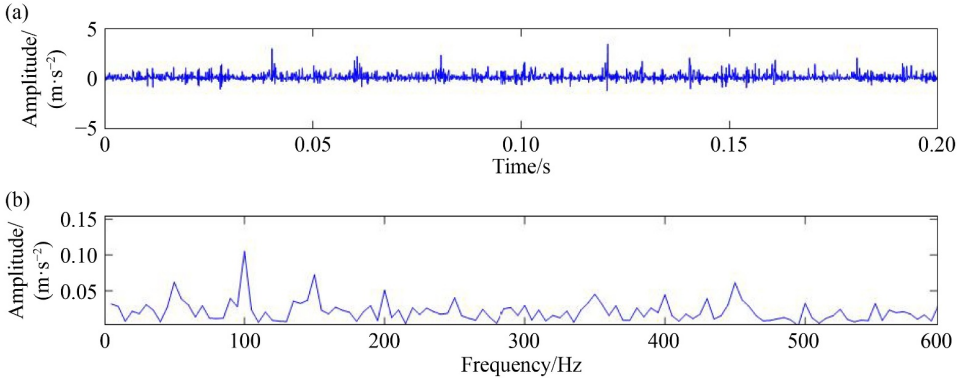


**Fig. 5** Analysis result of weighting higher order energy operator fusion of simulated signal: (a) time waveform and (b) envelope spectrum.

## 5 Experimental verifications

To investigate further the effectiveness of the proposed strategy for enhancing the bearing fault feature, three cases based on our self-made experimental platform are considered. They include a bearing signal with an outer race fault, a bearing signal with an inner race fault, and a bearing signal with a rolling element fault. Figure 7 shows that our self-made experimental platform consists of a motor, coupling, main shaft, and a loading system. The tested bearings (model#: SKF 6205-2RS) are installed at the right end of the main shaft. The

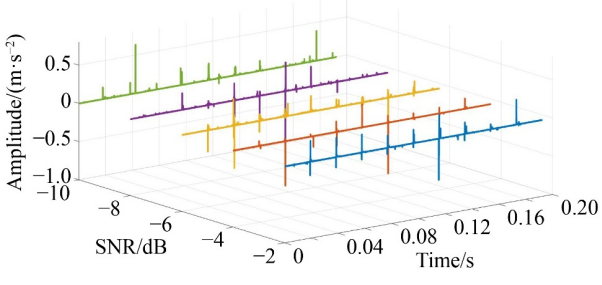


**Fig. 6** Fused results of the simulated signals with different SNRs. SNR: signal-to-noise ratio.

geometrical parameters of these bearings are provided in Table 1. The defect sizes of the three types of bearing faults are 0.2 mm generated by the electrical discharge machining. An accelerometer (model#: PCB 352C03, sensitivity: 50 mv/$g$, measuring range: ±10$g$) is installed to collect the vibration data with sampling rates of 10 kHz. In the process of data acquisition, the driven motor runs at a rotating speed of 1017 r/min. Therefore, the theoretical fault characteristic frequencies of the tested bearings are calculated as reported in Table 1, where $f_o$, $f_i$, and $f_b$ denote the ball pass frequency outer race, ball pass frequency inner race, and ball fault frequency, respectively.

### 5.1 Case of outer race fault

In this section, a bearing signal with an outer race fault is initially analyzed by the proposed strategy. Figure 8 shows the time waveform and envelope spectrum of the original signal. Some impulses are exhibited in the time waveform. However, the background noise is very strong. Thus, the harmonic components of the fault characteristic frequency in the envelope spectrum are not prominent enough. Then, the proposed strategy is employed to enhance the outer race fault feature. The parameters used in the proposed strategy are the same as those given in the analysis of simulated signals. Figure 9 depicts the relationship between the PE and the nearest neighboring size. As a result, the optimal fused result is obtained at the nearest neighboring size $k = 34$. Figure 10 presents the time waveform and envelope spectrum of the optimal fused result. The repetitive transients with the interval of $\Delta t_2 = 0.016$ s are uncovered in the time waveform effectively. The outer race fault frequency and its harmonics are exhibited in the envelope spectrum of the fused result clearly. These results indicate that the outer race fault exists at the tested bearing.

For comparing purposes, the processing results of

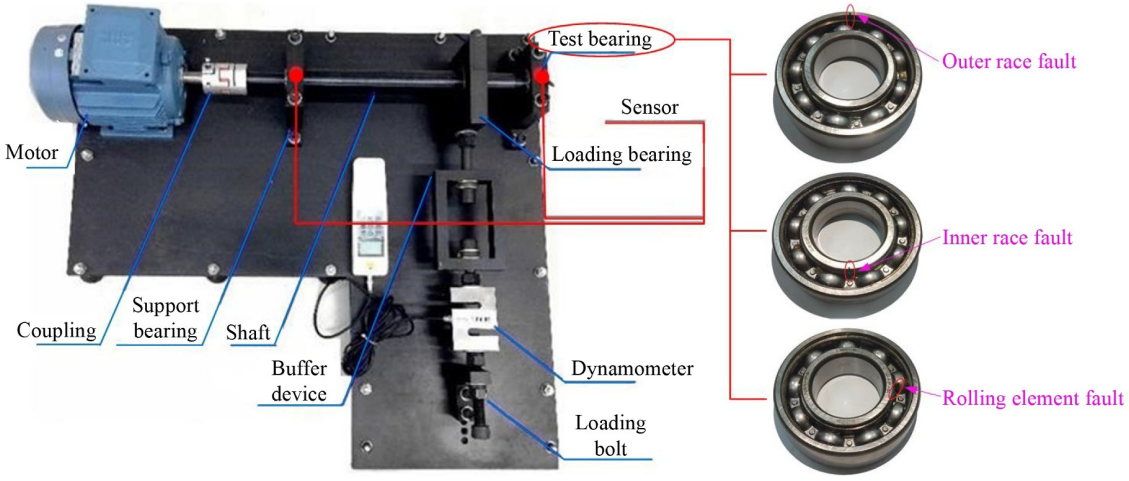


**Fig. 7** Test rig of rolling element bearing.

**Table 1** Geometrical parameters and fault characteristic frequencies of the experiment bearings

| Bearing model | Ball number | Ball diameter | Pitch diameter | $f_o$ | $f_i$ | $f_b$ |
|---|---|---|---|---|---|---|
| SKF 6205-2RS | 9 | 7.94 mm | 39.04 mm | 60.76 Hz | 91.79 Hz | 39.95 Hz |

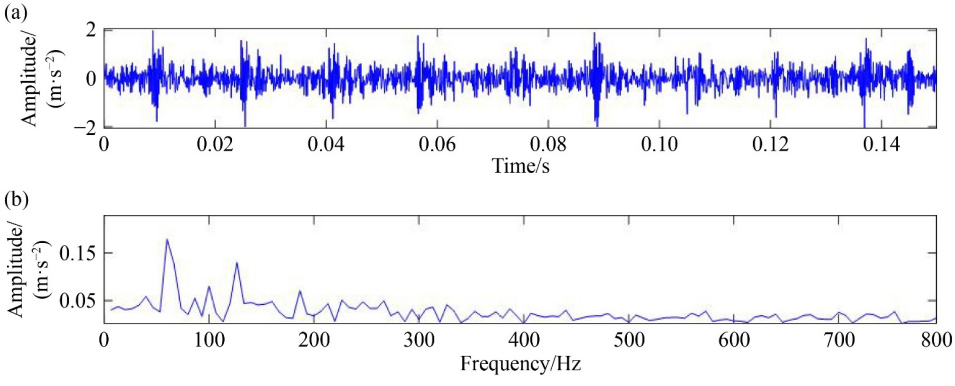


**Fig. 8** Bearing signal with an outer race fault: (a) time waveform and (b) envelope spectrum.

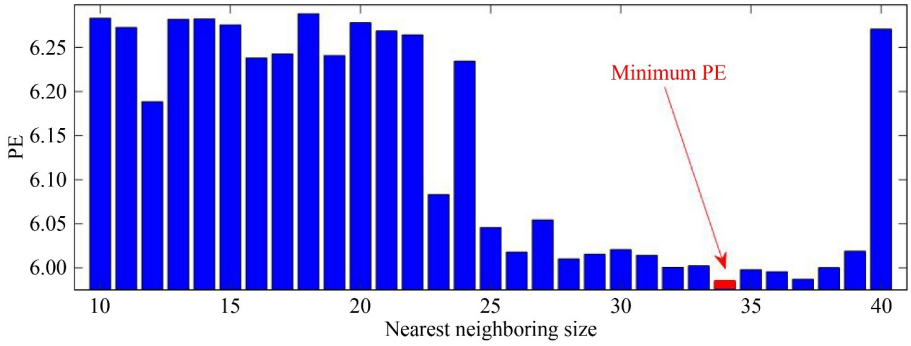


**Fig. 9** PE values of fused results of bearing signal with an outer race fault under different nearest neighboring sizes. PE: permutation entropy.

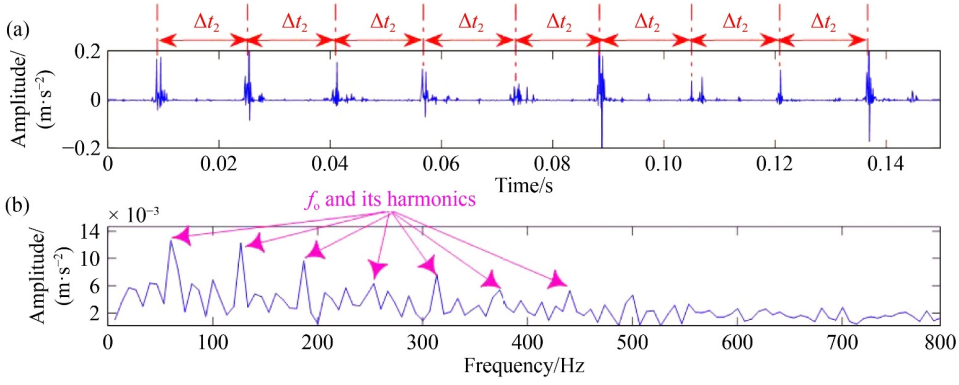


**Fig. 10** Fusion result of bearing signal with an outer race fault: (a) time waveform and (b) envelope spectrum.

HOEOs with the orders from 2 to 6 and their linearly fused result by the WHOEOF method are used to investigate the improved performance of the proposed strategy in enhancing the bearing fault feature. As shown in Fig. 11, the transients contained in the bearing signal with an outer race fault are enhanced by these HOEOs. Moreover, the envelope spectrum of the linearly fused result presents the outer race fault frequency and its harmonics in Fig. 12. Undeniably, the HOEOs and their linearly fused result have the ability to extract the outer race fault signatures to some extent. However, through visual inspection, the transients extracted by these two methods are still corrupted by noise. In addition, apparent interference frequencies occur when compared with the envelope spectrum obtained by the proposed strategy. Therefore, the proposed strategy is superior to the two comparing methods in the enhancement of the outer bearing defect.

Moreover, the fast Kurtogram (FK) algorithm [56] and the empirical mode decomposition (EMD) [57] are applied to analyze the same bearing signal with an outer race fault, respectively. The paving of FK is drawn in Fig. 13(a), where an optimal filter with a center frequency ($f_c$) of 4166.7 Hz and a bandwidth ($w_b$) of 1666.7 Hz is located. The waveform and envelope spectrum of the optimal filtered signal are demonstrated in Figs. 13(b) and 13(c), respectively. Although some transients can be observed from the waveform of the optimal filtered signal, the noises surrounded with these transients are more evident than those of the proposed strategy. Moreover, the harmonics of outer race fault frequency are also not obvious enough compared with those of the proposed strategy. The analysis results of the EMD method are given in Fig. 14. Figure 14 shows that all of the envelope spectra of the first four modes obtained by the EMD method deliver the outer race fault frequency, which is caused by the phenomenon of mode mixing in this method. Moreover, various interferences occur in the envelope spectra of the first four modes. Therefore, the proposed strategy has better ability for outer race fault extraction than those of FK and EMD.

To demonstrate the superiority of the proposed strategy further, a quantitative comparison is performed in all the comparing methods. Considering that the normalized frequency energy ratio (NFER) reflects the ratio between the fault characteristics and the interferences [58], it is selected as a quantitative measure as follows:

$$\mathrm{NFER} = 10\lg \frac{(K-H)\sum_{i=1}^{H} p(i\cdot f_{\mathrm{d}})}{\sum_{f=0}^{Hf_{\mathrm{d}}} p(f) - \sum_{i=1}^{H} p(i\cdot f_{\mathrm{d}})}, \tag{32}$$

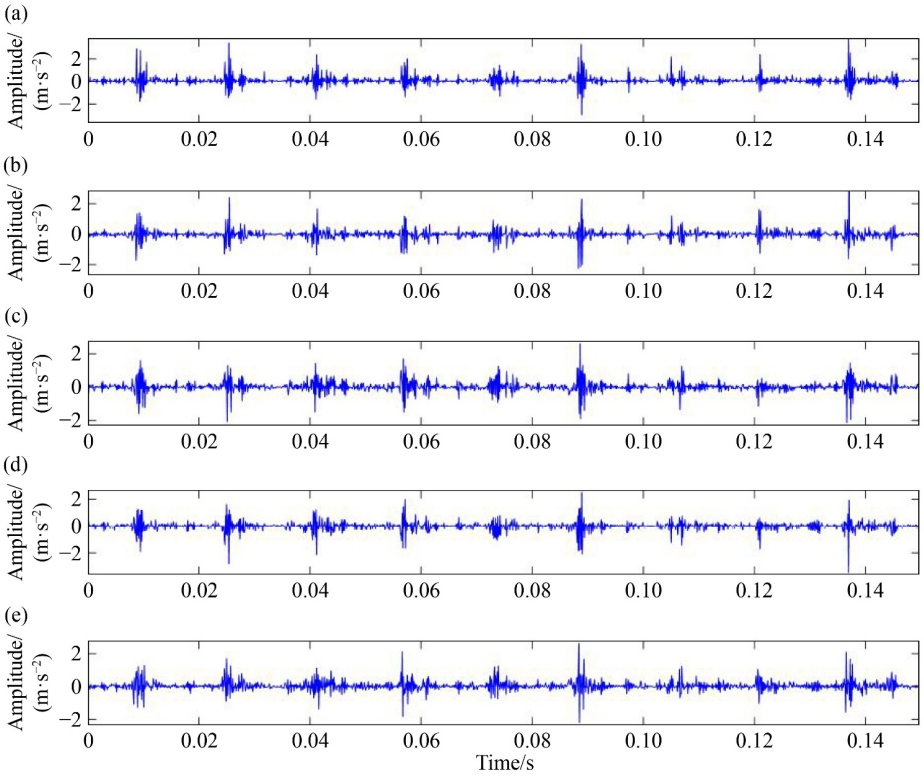


**Fig. 11** Results of higher order energy operators of bearing signal with an outer race fault: (a) order 2, (b) order 3, (c) order 4, (d) order 5, and (e) order 6.

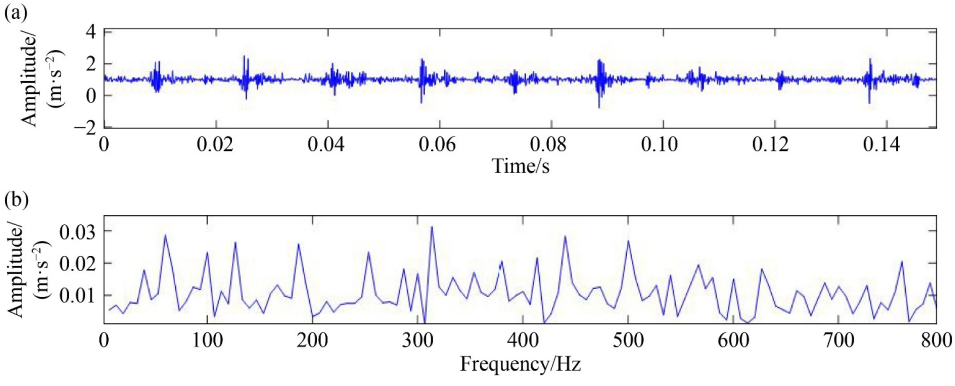


**Fig. 12** Analysis result of weighting higher order energy operator fusion of bearing signal with an outer race fault: (a) time waveform and (b) envelope spectrum.

where $f_d$ represents the corresponding fault characteristic frequency, $p(f)$ is the amplitude of the envelope spectrum at frequency $f$, $H$ stands for the number of harmonics used to calculate NFER, which is set as 3 in this study, $K$ denotes the number of spectral lines between 0 and $Hf_d$.

Figure 15 presents the NFERs of the envelope spectra of the bearing signal with an outer race fault obtained by the proposed strategy, WHOEOF, FK, and the first four modes of EMD. Evidently, the proposed strategy achieves the best result for characterizing the bearing outer race fault in all these comparing methods.

### 5.2 Case of inner race fault

In this case, a bearing signal with an inner race fault is analyzed by the proposed strategy. Figure 16 shows the waveform and envelope spectrum of the bearing signal, respectively. The transients contained in the original signal are seriously corrupted by the background noise. Thus, the harmonics of the inner race fault frequency in the envelope spectrum are not evident. To locate the fault position accurately, the clear repetitive transients should be effectively extracted. Then, the proposed strategy is applied to analyze the bearing signal with an inner race

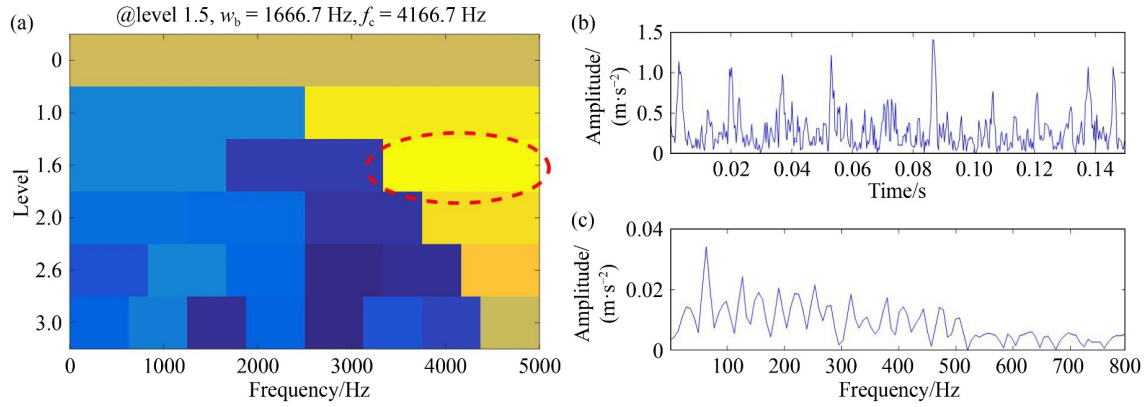


**Fig. 13** Results of fast Kurtogram of bearing signal with an outer race fault: (a) Kurtogram, (b) envelope waveform of the optimal filtered signal, and (c) envelope spectrum of the optimal filtered signal.

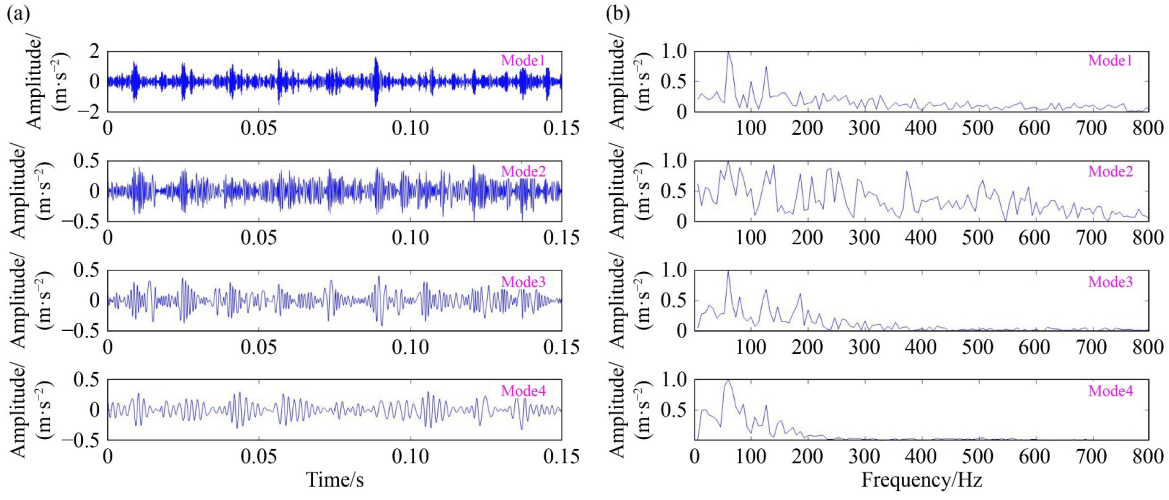


**Fig. 14** Results of empirical mode decomposition of bearing signal with an outer race fault: (a) waveforms of the first four modes and (b) envelope spectra of the first four modes.

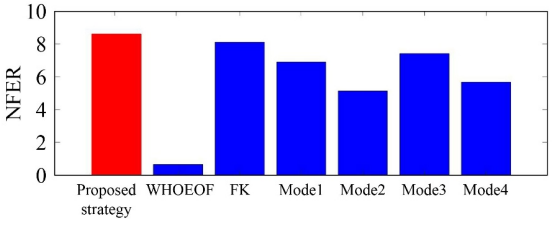


**Fig. 15** NFERs of the bearing signal with an outer race fault. NFER: normalized frequency energy ratio, WHOEOF: weighting higher order energy operator fusion, FK: fast Kurtogram. Mode1–Mode4 denote the first four modes of empirical mode decomposition.

fault. The parameters in the proposed strategy are also the same as those given in the previous cases. The nearest neighboring size $k$ from 10 to 40 is scanned to find the optimal one that has the minimum PE value. Figure 17 demonstrates that the PE reaches its minimal value at $k = 22$. Applying the proposed strategy with the optimal nearest neighboring size for nonlinear manifold learning, the final fused result can be obtained, as shown in Fig. 18(a). The results reveal clearer repetitive transients with the interval of $\Delta t_3 = 0.011$ s than the original bearing signal. Figure 18(b) shows the envelope spectrum of the fused result. The envelope spectrum shows that the inner race fault frequency and its harmonics are exhibited clearly. This result suggests that the defect on the inner race of the experimental bearing is effectively detected by the proposed strategy.

For comparison, the HOEOs with the orders from 2 to 6 and their linearly fused method with WHOEOF are employed to analyze the same bearing signal with an inner race fault. Figure 19 shows the processing results of the HOEOs with the different orders. Although the transients seem to be enhanced by these HOEOs, the repetitive transients cannot be observed, and the heavy noise still exists in the processing results of the HOEOs. In addition, Fig. 20 depicts the linearly fused result of the HOEOs by the WHOEOF method. Only two impulses protrude from the fused result, and no regular harmonic

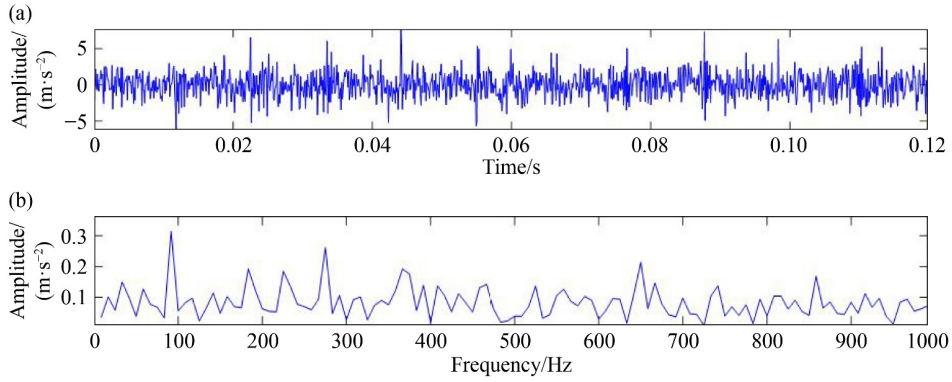


**Fig. 16** Bearing signal with an inner race fault: (a) time waveform and (b) envelope spectrum.

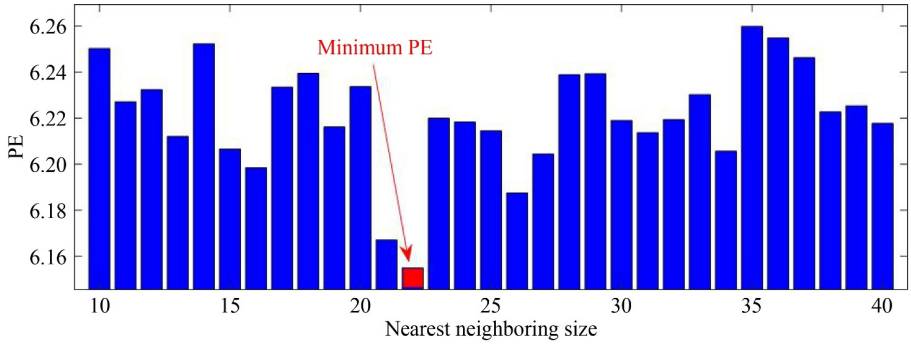


**Fig. 17** PE values of fused results of bearing signal with an inner race fault under different nearest neighboring sizes. PE: permutation entropy.

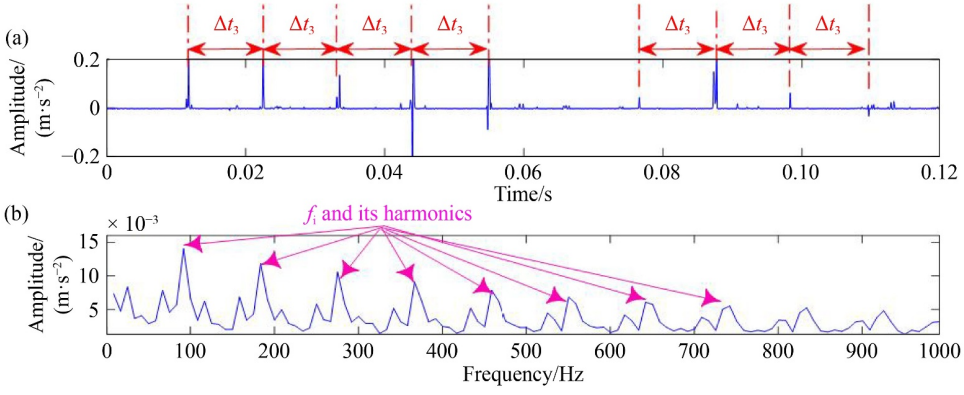


**Fig. 18** Fusion result of bearing signal with an inner race fault: (a) time waveform and (b) envelope spectrum.

of the inner race fault frequency exists in the envelope spectrum of the fused result. Therefore, the proposed strategy is more effective than the other two comparing methods in the fault characteristic identification of bearing with the inner race fault.

The bearing signal with an inner race fault is further analyzed by FK and EMD, respectively. The paving of FK is shown in Fig. 21(a), in which an optimal filter with a center frequency of 4687.5 Hz and a bandwidth of 625 Hz is automatically determined. Figures 21(b) and 21(c) illustrate the optimal filtered signal and its envelope spectrum, respectively. Although the envelope spectrum shows the inner race fault frequency of the tested bearing, the transients in the optimal filtered signal are not distributed regularly. The analysis results decomposed by EMD are shown in Fig. 22. The envelope spectra of the first mode and third mode obtained by EMD exhibit the inner race fault frequency. However, the waveforms of these modes confront severe background noise. These results indicate that the performance of the proposed

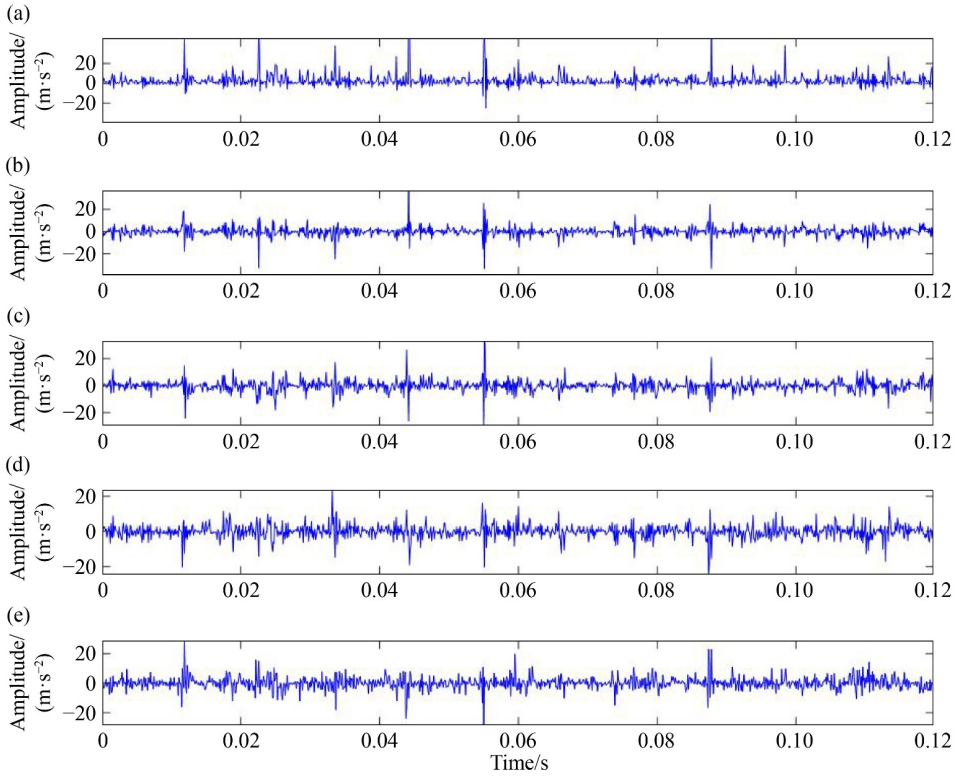


**Fig. 19** Results of higher order energy operators of bearing signal with an inner race fault: (a) order 2, (b) order 3, (c) order 4, (d) order 5, and (e) order 6.

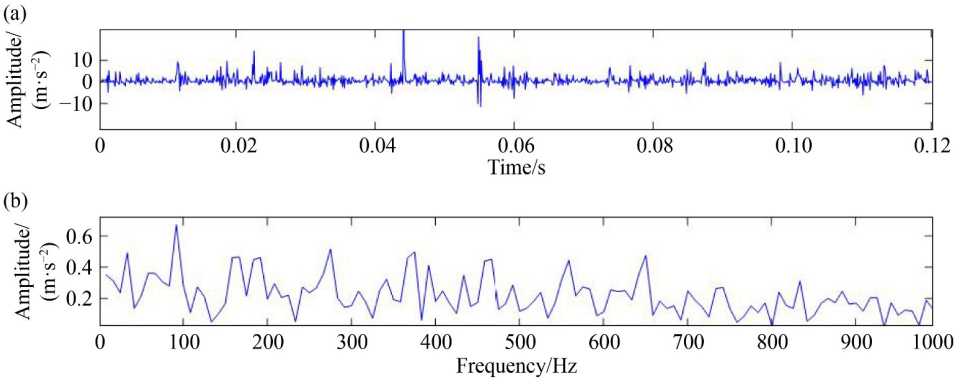


**Fig. 20** Analysis result of weighting higher order energy operator fusion of bearing signal with an inner race fault: (a) time waveform and (b) envelope spectrum.

strategy is superior to those of FK and EMD for bearing outer race fault extraction.

The NFERs of the envelope spectra of the bearing signal with an inner race fault obtained by the proposed strategy, WHOEOF, FK, and the first four modes of EMD are calculated to demonstrate the advancement of the proposed strategy quantitatively. Figure 23 shows the NFERs of different methods, in which the envelope spectrum of the proposed strategy has the largest NFER, that is, the proposed strategy delivers the optimal performance for characterizing the bearing inner race fault.

### 5.3 Case of rolling element fault

To confirm the enhanced performance of the proposed strategy in identifying the bearing fault feature further, a bearing signal with a rolling element fault is introduced here for analysis. Figure 24 shows the time waveform and envelope spectrum of the original bearing signal with a rolling element fault. The transients buried in the bearing signal are disturbed by the heavy noise in the time waveform. Hence, the dominant component is not at the rolling element fault frequency as shown in the envelope spectrum of the original bearing signal. Then, the bearing

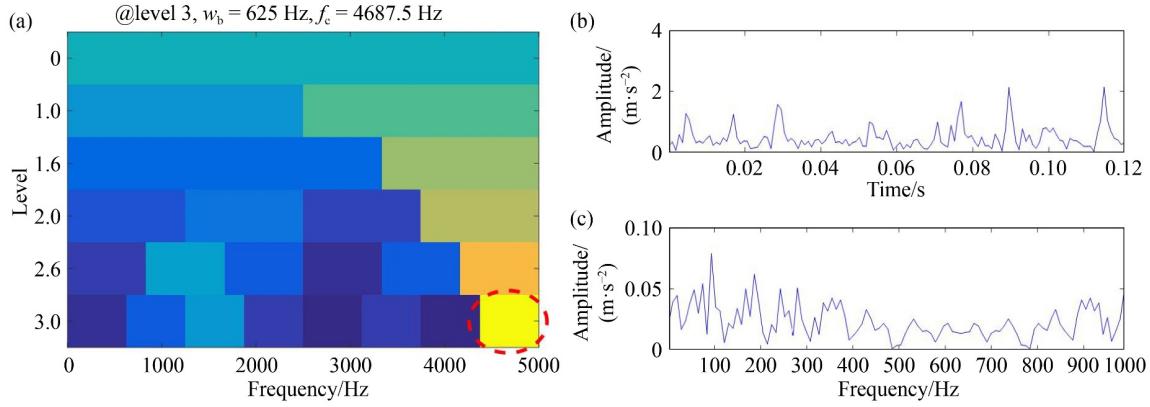


**Fig. 21** Results of fast Kurtogram of bearing signal with an inner race fault: (a) Kurtogram, (b) envelope waveform of the optimal filtered signal, and (c) envelope spectrum of the optimal filtered signal.

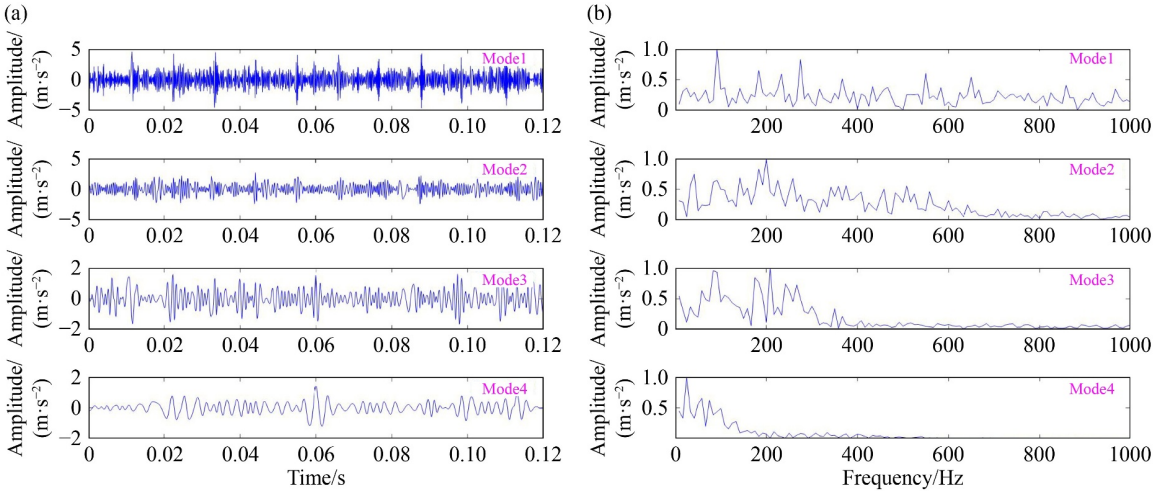


**Fig. 22** Results of empirical mode decomposition of bearing signal with an inner race fault: (a) waveforms of the first four modes and (b) envelope spectra of the first four modes.

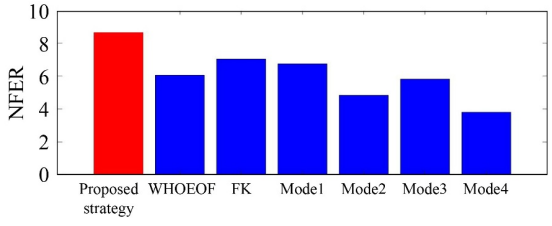


**Fig. 23** NFERs of the bearing signal with an inner race fault. NFER: normalized frequency energy ratio, WHOEOF: weighting higher order energy operator fusion, FK: fast Kurtogram. Mode1–Mode4 denote the first four modes of empirical mode decomposition.

signal with a rolling element fault is analyzed by the proposed strategy. Similarly, the parameters in the proposed strategy are also the same as those given in the above cases. The relationship between the PE and the nearest neighboring size is plotted in Fig. 25. As a result, the optimal fused result is obtained at $k = 15$, as shown in Fig. 26. The pure transients with the interval of $\Delta t_4 = 0.013$ s are recovered in the waveform of the optimal fused result. The envelope spectrum of the optimal fused result shows the rolling element fault frequency and its harmonics clearly. Notably, the rolling element fault frequency is always counted as two times because the defect on the rolling element surface would impact the inner and outer races exciting two transients [59]. These results indicate that the proposed strategy can effectively detect the rolling element fault of the tested bearing.

To investigate the improved performance of the proposed strategy in enhancing the rolling element fault, the HOEOs with the orders from 2 to 6 and their linearly fused strategy are also employed to analyze the same bearing signal with a rolling element fault. Figure 27 shows the time waveforms of processing results obtained by the HOEOs with different orders. The strong noise of the original bearing signal is reduced to a certain extent in these processing results. However, some noise still exists around the transients induced by the bearing defect.

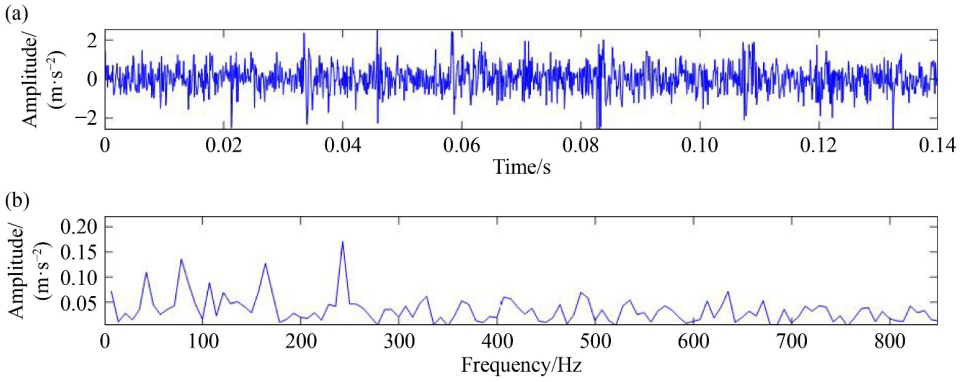


**Fig. 24** Bearing signal with a rolling element fault: (a) time waveform and (b) envelope spectrum.

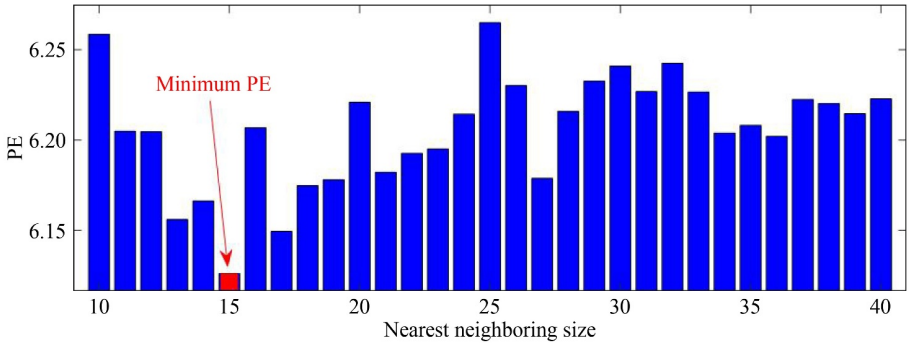


**Fig. 25** PE values of fused results of bearing signal with a rolling element fault under nearest neighboring sizes. PE: permutation entropy.

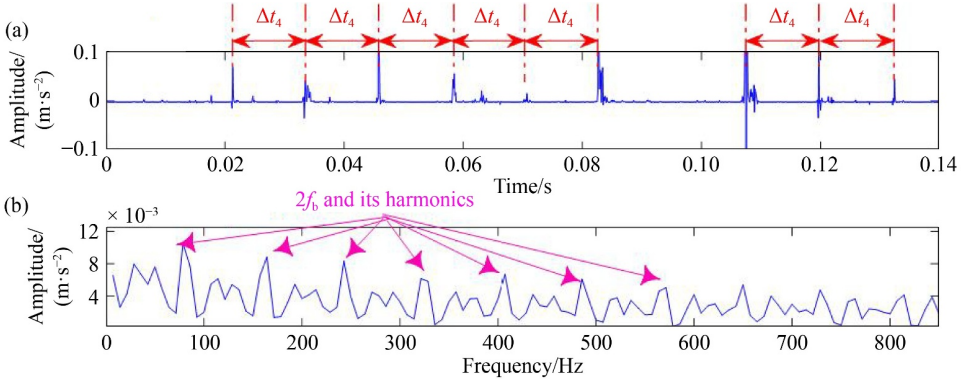


**Fig. 26** Fusion result of bearing signal with a rolling element fault: (a) time waveform and (b) envelope spectrum.

Figure 28 shows the fused result of these HOEOs by the WHOEOF method. The waveform of the fused result cannot deliver the regular transients induced by the rolling element defect. Meanwhile, as shown in the envelope spectrum of the fused result, the harmonics of the rolling element fault frequency are not evident compared with the result obtained by the proposed strategy. All of this evidence indicates that the proposed strategy can effectively capture the latent repetitive transients by fusing the HOEOs using manifold learning and has merits in noise suppression and impulse preserving.

For further comparison, FK and EMD are used to process the bearing signal with a rolling element fault. Figure 29 demonstrates the results obtained by FK, where Kurtogram indicates the optimal filter with a center frequency of 4687.5 Hz and a bandwidth of 625 Hz. The signal extracted by the optimal filter filtered and its envelope spectrum are drawn in Figs. 29(b) and 29(c). Evidently, the transients in the optimal filtered signal are a jumbled senseless mess. Moreover, Fig. 30 illustrates the analysis results of EMD. As shown in Fig. 30(a), the

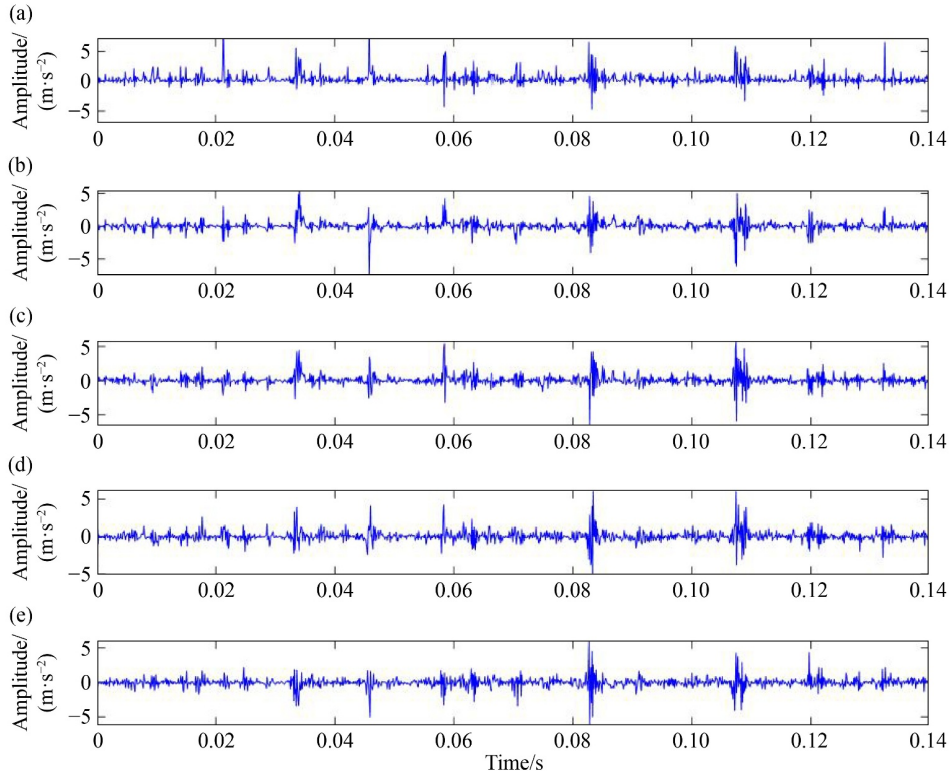


**Fig. 27** Results of higher order energy operators of bearing signal with a rolling element fault: (a) order 2, (b) order 3, (c) order 4, (d) order 5, and (e) order 6.

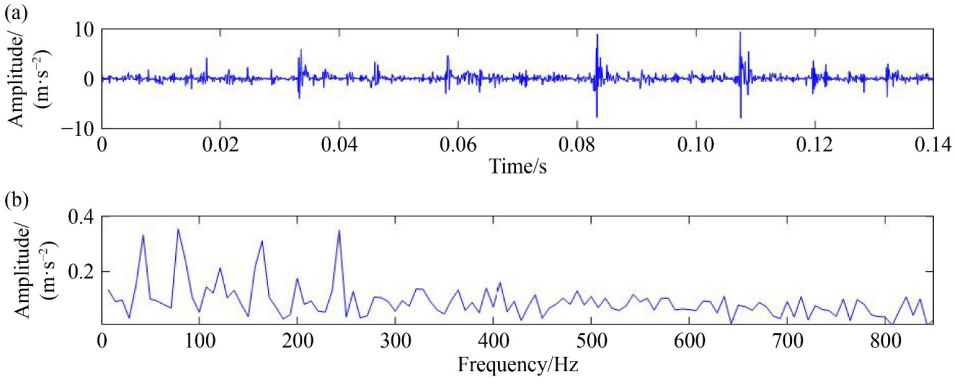


**Fig. 28** Analysis result of weighting higher order energy operator fusion of bearing signal with a rolling element fault: (a) time waveform and (b) envelope spectrum.

first four modes decomposed by EMD are contaminated by the strong noise. Various interferential frequencies occur in the envelope spectra of these decomposed modes. Therefore, the proposed strategy is more effective than all these comparing methods in the fault identification of a bearing signal with a rolling element fault.

Finally, to demonstrate the superiority of the proposed strategy quantitatively, the NFERs of the envelope spectra of the bearing signal with a rolling element fault obtained by all these methods are given in Fig. 31. The envelope spectrum obtained by the proposed strategy has the largest NFER. This evidence indicates that the proposed strategy has an excellent ability for bearing faulty feature extraction again.

## 6 Conclusions

Aiming at the shortcomings of EO and its variants in bearing fault detection, this study proposes an iterative HOEO fusion strategy for enhancing bearing defect identification. Two critical techniques, that is, the construction of MDIM and the enhanced manifold learning, are constructed in the proposed strategy. The

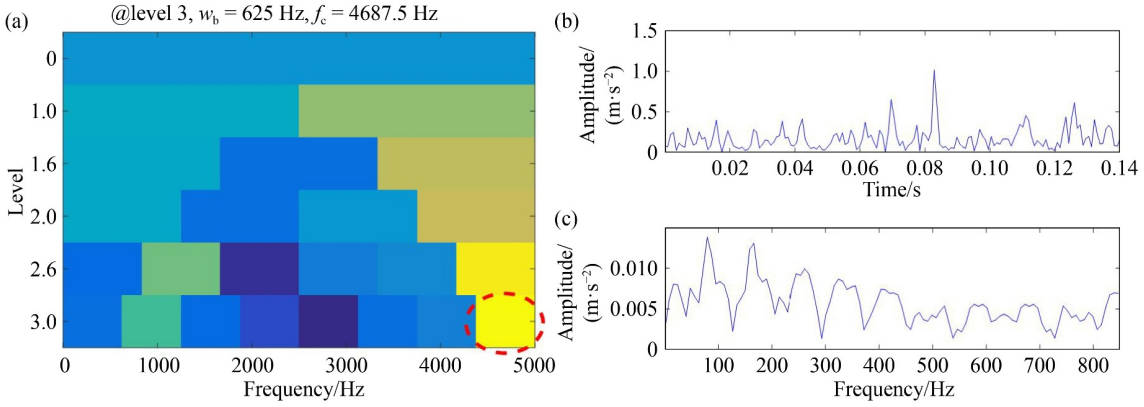


**Fig. 29** Results of fast Kurtogram of bearing signal with a rolling element fault: (a) Kurtogram, (b) envelope waveform of the optimal filtered signal, and (c) envelope spectrum of the optimal filtered signal.

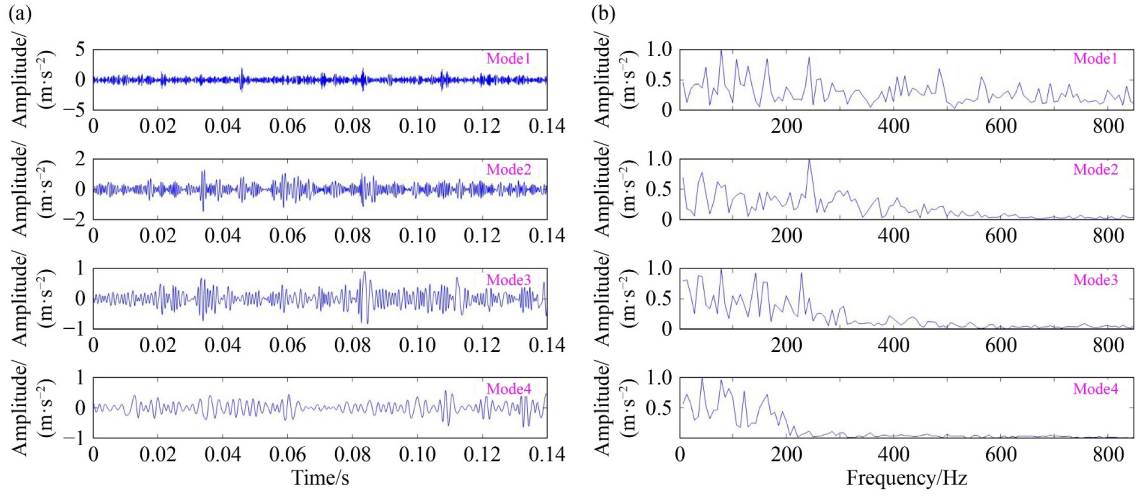


**Fig. 30** Results of empirical mode decomposition of bearing signal with a rolling element fault: (a) waveforms of the first four modes and (b) envelope spectra of the first four modes.

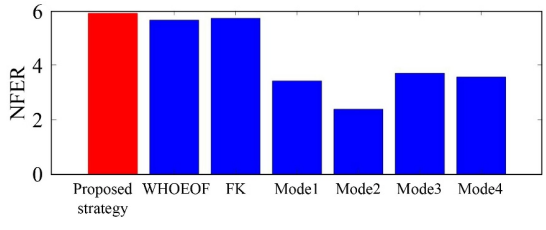


**Fig. 31** NFERs of the bearing signal with a rolling element fault. NFER: normalized frequency energy ratio, WHOEOF: weighting higher order energy operator fusion, FK: fast Kurtogram. Mode1–Mode4 denote the first four modes of empirical mode decomposition.

MDIM formulated by performing the HOEOs on the analysis signal iteratively can provide abundant sources for the fusion strategy and avoid the significant amplification of the high frequency with an oversized order of HOEO. The enhanced manifold learning is conducted on the MDIM, from which the LTSA algorithm is used to extract the buried intrinsic manifolds. Then, the eigenvalue weighting idea is designed to combine these intrinsic manifolds. Notably, manifold learning is a typically nonlinear fusion method, which has the merit of in-band noise reduction. The proposed iterative HOEO fusion strategy has been successfully applied to analyze the simulated signal and the bearing experimental signals with outer race, inner race, and rolling element faults. The effectiveness and superiority of the proposed iterative HOEO fusion strategy over HOEOs, WHOEOF, FK, and EMD have been confirmed by the analysis results, thus proving that this tool is promising for enhancing the bearing fault feature.

## Nomenclature

Abbreviations

| | |
|---|---|
| EMD | Empirical mode decomposition |

| | |
|---|---|
| EO | Energy operator |
| FK | Fast Kurtogram |
| HOEO | Higher order energy operator |
| LTSA | Local tangent space alignment |
| MDIM | Multi-dimensional information matrix |
| NFER | Normalized frequency energy ratio |
| PE | Permutation entropy |
| REB | Rolling element bearing |
| SIR | Signal-to-interference ratio |
| SNR | Signal-to-noise ratio |
| WHOEOF | Weighting higher order energy operator fusion |

## Variables

| | |
|---|---|
| $A$ | Amplitude of the fault bearing vibration |
| $\boldsymbol{A}$ | Alignment matrix |
| $\boldsymbol{C}_i$ | Correlation matrix |
| $\mathrm{E}_j[\cdot]$ | Function of the $j$th order EO |
| Envsq[·] | Function of squared envelope |
| $\boldsymbol{e}_k$ | Column vector of $k$ ones |
| $f_\mathrm{b}$ | Rolling element fault frequency |
| $f_\mathrm{c}$ | Center frequency |
| $f_\mathrm{d}$ | Fault characteristic frequency |
| $f_\mathrm{i}$ | Inner race fault frequency |
| $f_\mathrm{o}$ | Outer race fault frequency |
| $f_\mathrm{RE}$ | Resonance frequency |
| $\boldsymbol{g}_i$ | Eigenvector of the alignment matrix |
| $\boldsymbol{G}$ | Reorganizing result of the global representation $\boldsymbol{G}_0$ |
| $\boldsymbol{G}_0$ | Global representation of manifold learning |
| $H$ | Number of harmonics used to calculate NFER |
| HOEO-F(·) | Function of WHOEOF |
| $Id$ | Number of the saved intrinsic dimensions |
| $\boldsymbol{I}$ | Identity matrix |
| $J$ | Total number of orders |
| $k$ | Nearest neighboring size |
| $k^*$ | Nearest neighborhood corresponding to the smallest $P$ |
| $K$ | Number of spectral lines |
| Kurt(·) | Function of kurtosis |
| $L_j$ | Amplitude of the $j$th interference component |
| $m$ | Embedded dimension |
| $\boldsymbol{M}$ | MDIM |
| $\overline{\boldsymbol{M}}$ | Normalized MDIM |
| $\boldsymbol{M}(x(t))$ | MDIM with the signal $x(t)$ |
| $\boldsymbol{M}_1(x(t))$ | HOEO matrix of signal $x(t)$ |
| $\boldsymbol{M}_2(x(t))$ | Once iterative of $\boldsymbol{M}_1(x(t))$ |
| $\boldsymbol{M}_3(x(t))$ | Twice iterative of $\boldsymbol{M}_1(x(t))$ |
| $n(t)$ | Noise component |
| $N$ | Number of data points of the analysis signal |
| $p(f)$ | Amplitude of the envelope spectrum at frequency $f$ |
| $P_i$ | Relative frequency of the $i$th permutation |
| $P_k$ | PE of the reorganizing result $G$ at nearest neighbors $k$ |
| $r(t)$ | Fault bearing vibration |
| $\boldsymbol{R}_i$ | Row vector of the MDIM |
| $\overline{\boldsymbol{R}}_i$ | Row vector of the normalized MDIM |
| S($t$) | A transient with unit amplitude |
| $\boldsymbol{R}_i$ | 0-1 selection matrix |
| SIR(·) | Function of SIR |
| $t$ | Time |
| $T$ | Total lasting time of analysis signal |
| $T_\mathrm{d}$ | Time interval between two adjacent transients |
| $T_\mathrm{p}$ | Time period of the fault characteristic frequency |
| $\Delta t_1$, $\Delta t_2$, $\Delta t_3$, $\Delta t_4$ | Intervals of the repetitive transients in the simulated bearing, outer race, inner race, and rolling element fault signal, respectively |
| $u_j(t)$ | $j$th vibration interferences |
| $\boldsymbol{V}_i$ | Matrix composed by $Id$ largest right singular vectors of centralized matrix |
| $w_\mathrm{b}$ | Bandwidth |
| $x(t)$ | Continuous time signal |
| $x(n)$ | Discrete form of $x(t)$ |
| $\dot{x}(t)$ | First-order derivative of $x(t)$ with respect to time $t$ |
| $\hat{\dot{x}}(t)$ | Hilbert transform of $\dot{x}(t)$ |
| $\ddot{x}(t)$ | Second-order derivative of $x(t)$ with respect to time $t$ |
| $x^{(j)}(t)$ | $j$th derivative of $x(t)$ |
| $y(t)$ | Preset transients |
| $\boldsymbol{Z}_i$ | Matrix combined by a set of $k$ nearest neighbors of column $\boldsymbol{m}_n$ |
| $\overline{\boldsymbol{Z}}_i$ | Mean of $\boldsymbol{Z}_i$ |
| $\alpha_j$ | Coefficient associated with the $j$th HOEO |
| $\alpha_j^*$ | Optimal coefficient associated with the $j$th HOEO |
| $\boldsymbol{\alpha}^*$ | Optimal coefficient vector |
| $\beta$ | Structural damping characteristic of the fault bearing vibration |
| $\omega_j$ | Frequency of the $j$th interference component |
| $\omega_\mathrm{r}$ | Resonance frequency excited by the bearing defect |
| $\lambda_i$ | Eigenvalue of the alignment matrix |
| $\xi$ | Decay rate of the transient |
| $\tau_i$ | A random variable to simulate the slip effect of transients |

**Acknowledgements** The authors declare that they have no competing financial interests or personal relationships that could have appeared to influence the work reported in this paper. This research was supported by the National Natural Science Foundation of China (Grant Nos. 52172406 and 51875376), the China Postdoctoral Science Foundation (Grant Nos. 2022T150552 and 2021M702752), and the Suzhou Prospective Research

Program, China (Grant No. SYG202111), which are highly appreciated by the authors.

## References


1. An Z H, Jiang X X, Cao J, Yang R, Li X G. Self-learning transferable neural network for intelligent fault diagnosis of rotating machinery with unlabeled and imbalanced data. Knowledge-Based Systems, 2021, 230: 107374
2. Chen X F, Wang S B, Qiao B J, Chen Q. Basic research on machinery fault diagnostics: past, present, and future trends. Frontiers of Mechanical Engineering, 2018, 13(2): 264–291
3. Wang X, Gu H Y, Wang T Y, Zhang W, Li A H, Chu F L. Deep convolutional tree-inspired network: a decision-tree-structured neural network for hierarchical fault diagnosis of bearings. Frontiers of Mechanical Engineering, 2021, 16(4): 814–828
4. Zhang X, Huang T, Wu B, Hu Y M, Huang S, Zhou Q, Zhang X. Multi-model ensemble deep learning method for intelligent fault diagnosis with high-dimensional samples. Frontiers of Mechanical Engineering, 2021, 16(2): 340–352
5. Liu J, Zhou K B, Yang C Y, Lu G L. Imbalanced fault diagnosis of rotating machinery using autoencoder-based SuperGraph feature learning. Frontiers of Mechanical Engineering, 2021, 16(4): 829–839
6. Ziaja A, Antoniadou I, Barszcz T, Staszewski W J, Worden K. Fault detection in rolling element bearings using wavelet-based variance analysis and novelty detection. Journal of Vibration and Control, 2016, 22(2): 396–411
7. Syed S H, Muralidharan V. Feature extraction using discrete wavelet transform for fault classification of planetary gearbox—a comparative study. Applied Acoustics, 2022, 188: 108572
8. An B T, Wang S B, Yan R Q, Li W H, Chen X F. Adaptive robust noise modeling of sparse representation for bearing fault diagnosis. IEEE Transactions on Instrumentation and Measurement, 2021, 70: 1–12
9. Ahmed H O A, Wong M L D, Nandi A K. Intelligent condition monitoring method for bearing faults from highly compressed measurements using sparse over-complete features. Mechanical Systems and Signal Processing, 2018, 99: 459–477
10. Xiao L, Bajric R, Zhao J S, Tang J X, Zhang X H. An adaptive vibrational resonance method based on cascaded varying stable-state nonlinear systems and its application in rotating machine fault detection. Nonlinear Dynamics, 2021, 103(1): 715–739
11. López C, Naranjo Á, Lu S L, Moore K J. Hidden markov model based stochastic resonance and its application to bearing fault diagnosis. Journal of Sound and Vibration, 2022, 528: 116890
12. Lu S L, Zheng P, Liu Y B, Cao Z, Yang H, Wang Q J. Sound-aided vibration weak signal enhancement for bearing fault detection by using adaptive stochastic resonance. Journal of Sound and Vibration, 2019, 449: 18–29
13. Abdelkader R, Kaddour A, Bendiabdellah A, Derouiche Z. Rolling bearing fault diagnosis based on an improved denoising method using the complete ensemble empirical mode decomposition and the optimized thresholding operation. IEEE Sensors Journal, 2018, 18(17): 7166–7172
14. Jiang X X, Huang Q, Shen C Q, Wang Q, Xu K, Liu J, Shi J J, Zhu Z K. Synchronous chirp mode extraction: a promising tool for fault diagnosis of rolling element bearings under varying speed conditions. Chinese Journal of Aeronautics, 2022, 35(1): 348–364
15. Jiang X X, Song Q Y, Wang H E, Du G F, Guo J F, Shen C Q, Zhu Z K. Central frequency mode decomposition and its applications to the fault diagnosis of rotating machines. Mechanism and Machine Theory, 2022, 174: 104919
16. Jiang X X, Wang J, Shen C Q, Shi J J, Huang W G, Zhu Z K, Wang Q. An adaptive and efficient variational mode decomposition and its application for bearing fault diagnosis. Structural Health Monitoring, 2021, 20(5): 2708–2725
17. Maurya S, Singh V, Verma N K. Condition monitoring of machines using fused features from EMD-based local energy with DNN. IEEE Sensors Journal, 2020, 20(15): 8316–8327
18. Liang M, Bozchalooi I S. An energy operator approach to joint application of amplitude and frequency-demodulations for bearing fault detection. Mechanical Systems and Signal Processing, 2010, 24(5): 1473–1494
19. Liu Y, Jiang Z S, Huang H Z, Xiang J W. A TEO-based modified laplacian of gaussian filter to detect faults in rolling element bearing for variable rotational speed machine. IET Science, Measurement & Technology, 2021, 15(2): 193–203
20. Wan S T, Zhang X. Bearing fault diagnosis based on Teager energy entropy and mean-shift fuzzy C-means. Structural Health Monitoring, 2020, 19(6): 1976–1988
21. Han T, Liu Q N, Zhang L, Tan A C C. Fault feature extraction of low speed roller bearing based on Teager energy operator and CEEMD. Measurement, 2019, 138: 400–408
22. Ma J, Wu J D, Wang X D. Incipient fault feature extraction of rolling bearings based on the MVMD and Teager energy operator. ISA Transactions, 2018, 80: 297–311
23. Gu R, Chen J, Hong R J, Wang H, Wu W W. Incipient fault diagnosis of rolling bearings based on adaptive variational mode decomposition and Teager energy operator. Measurement, 2020, 149: 106941
24. Feng Z P, Zuo M J, Hao R J, Chu F L, Lee J. Ensemble empirical mode decomposition-based teager energy spectrum for bearing fault diagnosis. Journal of Vibration and Acoustics, 2013, 135(3): 031013
25. Singh J, Darpe A K, Singh S P. Rolling element bearing fault diagnosis based on over-complete rational dilation wavelet transform and auto-correlation of analytic energy operator. Mechanical Systems and Signal Processing, 2018, 100: 662–693
26. Pei X L, Zheng X Y, Wu J L. Intelligent bearing fault diagnosis based on Teager energy operator demodulation and multiscale compressed sensing deep autoencoder. Measurement, 2021, 179: 109452
27. Chen Z X, He C B, Liu Y B, Lu S L, Liu F, Li G L. Incipient fault feature extraction of rolling bearing based on optimized singular spectrum decomposition. IEEE Sensors Journal, 2021, 21(18): 20362–20374
28. Zeng M, Yang Y, Zheng J D, Cheng J S. Normalized complex Teager energy operator demodulation method and its application to fault diagnosis in a rubbing rotor system. Mechanical Systems and

Signal Processing, 2015, 50–51: 380–399
29. Randall R B, Smith W A. Uses and mis-uses of energy operators for machine diagnostics. Mechanical Systems and Signal Processing, 2019, 133: 106199
30. Liang M, Faghidi H. A non-parametric non-filtering approach to bearing fault detection in the presence of multiple interference. Measurement Science and Technology, 2013, 24(10): 105013
31. Liang M, Faghidi H. Intelligent bearing fault detection by enhanced energy operator. Expert Systems with Applications, 2014, 41(16): 7223–7234
32. Imaouchen Y, Kedadouche M, Alkama R, Thomas M. A frequency-weighted energy operator and complementary ensemble empirical mode decomposition for bearing fault detection. Mechanical Systems and Signal Processing, 2017, 82: 103–116
33. O'Toole J M, Temko A, Stevenson N. Assessing instantaneous energy in the EEG: a non-negative, frequency-weighted energy operator. In: Proceedings of the 36th Annual International Conference of the IEEE Engineering in Medicine and Biology Society. Chicago: IEEE, 2014, 3288–3291
34. Jiang X X, Li S M, Cheng C. A novel method for adaptive multiresonance bands detection based on VMD and using MTEO to enhance rolling element bearing fault diagnosis. Shock and Vibration, 2016, 2016: 8361289
35. Feng Z P, Qin S F, Liang M. Time−frequency analysis based on Vold-Kalman filter and higher order energy separation for fault diagnosis of wind turbine planetary gearbox under nonstationary conditions. Renewable Energy, 2016, 85: 45–56
36. Xu Y B, Cai Z Y, Ding K. An enhanced bearing fault diagnosis method based on TVF-EMD and a high-order energy operator. Measurement Science and Technology, 2018, 29(9): 095108
37. Faghidi H, Liang M. Bearing fault identification by higher order energy operator fusion: a non-resonance based approach. Journal of Sound and Vibration, 2016, 381: 83–100
38. Faghidi H, Liang M. Detection of bearing fault detection from heavily contaminated signals: a higher-order analytic energy operator method. Journal of Vibration and Acoustics, 2015, 137(4): 041012
39. Maragos P, Potamianos A. Higher order differential energy operators. IEEE Signal Processing Letters, 1995, 2(8): 152–154
40. Wang J, Du G F, Zhu Z K, Shen C Q, He Q B. Fault diagnosis of rotating machines based on the EMD manifold. Mechanical Systems and Signal Processing, 2020, 135: 106443
41. Li Q C, Ding X X, He Q B, Huang W B, Shao Y M. Manifold sensing-based convolution sparse self-learning for defective bearing morphological feature extraction. IEEE Transactions on Industrial Informatics, 2021, 17(5): 3069–3078
42. Wang Y, Xu G H, Liang L, Jiang K S. Detection of weak transient signals based on wavelet packet transform and manifold learning for rolling element bearing fault diagnosis. Mechanical Systems and Signal Processing, 2015, 54–55: 259–276
43. Wang J, He Q B. Wavelet packet envelope manifold for fault diagnosis of rolling element bearings. IEEE Transactions on Instrumentation and Measurement, 2016, 65(11): 2515–2526
44. Wang J, He Q B, Kong F R. Multiscale envelope manifold for enhanced fault diagnosis of rotating machines. Mechanical Systems and Signal Processing, 2015, 52–53: 376–392
45. Hurley N, Rickard S. Comparing measures of sparsity. IEEE Transactions on Information Theory, 2009, 55(10): 4723–4741
46. Wang Y X, Xiang J W, Markert R, Liang M. Spectral kurtosis for fault detection, diagnosis and prognostics of rotating machines: a review with applications. Mechanical Systems and Signal Processing, 2016, 66–67: 679–698
47. Miao Y H, Zhao M, Lin J. Improvement of kurtosis-guided-grams via Gini index for bearing fault feature identification. Measurement Science and Technology, 2017, 28(12): 125001
48. Wang D, Zhong J J, Li C, Peng Z K. Box-Cox sparse measures: a new family of sparse measures constructed from kurtosis and negative entropy. Mechanical Systems and Signal Processing, 2021, 160: 107930
49. Hou B C, Wang D, Xia T B, Xi L F, Peng Z K, Tsui K L. Generalized Gini indices: complementary sparsity measures to Box-Cox sparsity measures for machine condition monitoring. Mechanical Systems and Signal Processing, 2022, 169: 108751
50. Hou B C, Wang D, Xia T B, Wang Y, Zhao Y, Tsui K L. Investigations on quasi-arithmetic means for machine condition monitoring. Mechanical Systems and Signal Processing, 2021, 151: 107451
51. Wang D. Some further thoughts about spectral kurtosis, spectral $L2/L1$ norm, spectral smoothness index and spectral Gini index for characterizing repetitive transients. Mechanical Systems and Signal Processing, 2018, 108: 360–368
52. Rostaghi M, Ashory M R, Azami H. Application of dispersion entropy to status characterization of rotary machines. Journal of Sound and Vibration, 2019, 438: 291–308
53. Wang X Z, Si S B, Li Y B. Multiscale diversity entropy: a novel dynamical measure for fault diagnosis of rotating machinery. IEEE Transactions on Industrial Informatics, 2021, 17(8): 5419–5429
54. Yan R Q, Liu Y B, Gao R X. Permutation entropy: a nonlinear statistical measure for status characterization of rotary machines. Mechanical Systems and Signal Processing, 2012, 29: 474–484
55. Randall R B, Antoni J. Rolling element bearing diagnostics—a tutorial. Mechanical Systems and Signal Processing, 2011, 25(2): 485–520
56. Antoni J. Fast computation of the kurtogram for the detection of transient faults. Mechanical Systems and Signal Processing, 2007, 21(1): 108–124
57. Lei Y G, Lin J, He Z J, Zuo M J. A review on empirical mode decomposition in fault diagnosis of rotating machinery. Mechanical Systems and Signal Processing, 2013, 35(1–2): 108–126
58. Song Q Y, Jiang X X, Wang S, Guo J F, Huang W G, Zhu Z K. Self-adaptive multivariate variational mode decomposition and its application for bearing fault diagnosis. IEEE Transactions on Instrumentation and Measurement, 2022, 71: 1–13
59. Huang Y, Lin J H, Liu Z C, Wu W Y. A modified scale-space guiding variational mode decomposition for high-speed railway bearing fault diagnosis. Journal of Sound and Vibration, 2019, 444: 216–234